THE JOURNAL OF PHYSICAL CHEMISTRY C

Article

Cite This: J. Phys. Chem. C 2017, 121, 24206-24222

pubs.acs.org/JPCC

Rapid Sonochemical Approach Produces Functionalized Fe_3O_4 Nanoparticles with Excellent Magnetic, Colloidal, and Relaxivity Properties for MRI Application

Davino M. A. Neto,[†] Rafael M. Freire,[‡] Juan Gallo,[§] Tiago M. Freire,[†] Danilo C. Queiroz,[∥] Nágila M. P. S. Ricardo,[∥] Igor F. Vasconcelos,[⊥] Giuseppe Mele,[#] Luigi Carbone,[▽] Selma E. Mazzetto,[∥] Manuel Bañobre-López,[§] and Pierre B. A. Fechine*[,†]

[†]Group of Chemistry of Advanced Materials (GQMAT)- Department of Analytical Chemistry and Physical Chemistry, Federal University of Ceará − UFC, Campus do Pici, Zip Code 60451-970, Fortaleza, Brazil

[‡]Department of Physics, Universidad de Santiago de Chile, USACH, Av. Ecuador 3493, Santiago, Chile

[§]Advanced (Magnetic) Theranostic Nanostructures Lab, International Iberian Nanotechnology Laboratory, Av. Mestre José Veiga, 4715-330 Braga, Portugal

[∥]Department of Organic and Inorganic Chemistry, Federal University of Ceará-UFC, Campus do Pici, 60451-970 Fortaleza, CE, Brazil

[⊥]Department of Metallurgic and Materials Engineering, Federal University of Ceará − UFC, Campus do Pici, 60451-970, Fortaleza, Brazil

[#]Dipartimento di Ingegneria dell'Innovazione, Università del Salento, Via Arnesano, 73100 Lecce, Italy

[▽]CNR NANOTEC-Istituto di Nanotecnologia, c/o Campus Ecotekne, Università del Salento, Via Monteroni, 73100 Lecce, Italy

Supporting Information

ABSTRACT: Functionalized Fe_3O_4 nanoparticles (NPs) have emerged as a promising contrast agent for magnetic resonance imaging (MRI). Their synthesis and functionalization methodology strongly affect their performance in vivo. The methodology most used in the literature for the synthesis of Fe_3O_4 NPs is thermal decomposition, which has proven to be time-consuming, expensive, and laborious, as it requires further ligand exchange strategies to transfer the as-synthesized nanoparticles from organic to aqueous solvents. This work describes a rapid and facile sonochemical methodology to synthesize and functionalize Fe_3O_4 NPs with excellent physicochemical properties for MRI. This sonochemistry approach was used to produce, in 12 min, Fe_3O_4 NPs functionalized with polysodium acrylate (PAANa), trisodium citrate (CIT), branched polyethylenimine (BPEI), and sodium oleate. X-ray diffraction and transmission electron microscopy demonstrated that the NPs were composed of a single inverse spinel phase with an average diameter of 9−11 nm and a narrow size distribution. Mössbauer spectroscopy and magnetic measurements confirmed that the obtained NPs were transitioning to the superparamagnetic regime and possessed excellent magnetization saturation values (59−77 emu/g). Fourier transform infrared spectroscopy proved that the sonochemistry approach provided conditions that induced a strong interaction between Fe_3O_4 and the coating agents. Furthermore, dynamic light-scattering experiments evidenced that samples coated with PAANa, CIT, and BPEI possess colloidal stability in aqueous solvents. Emphasis must be placed on PAANa-coated NPs, which also presented remarkable colloidal stability under simulated physiological conditions. Finally, the obtained NPs exhibited great potential to be applied as an MRI contrast agent. The transverse relaxivity values of the NPs synthesized in this work (277−439 $mM^{-1}\ s^{-1}$) were greater than those of commercial NPs and those prepared using other methodologies. Therefore, this work represents significant progress in the preparation of Fe_3O_4 NPs, providing a method to prepare high-quality materials in a rapid, cost-effective, and facile manner.

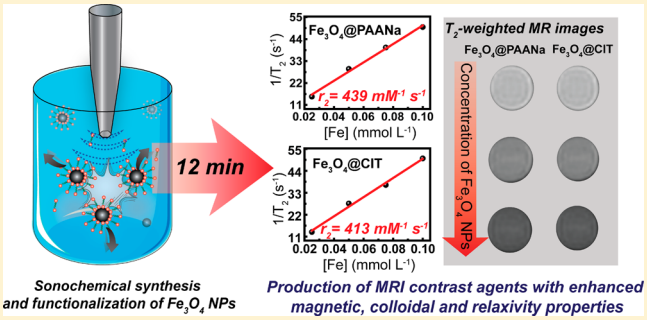

INTRODUCTION

Magnetic nanoparticles (MNPs) have introduced new possibilities into the diagnosis and treatment of cancer diseases, overcoming the drawbacks of conventional treatments.[1] These

Received: May 22, 2017
Revised: October 9, 2017
Published: October 10, 2017

DOI: 10.1021/acs.jpcc.7b04941
J. Phys. Chem. C 2017, 121, 24206−24222

MNPs can be used in drug and gene delivery,[2] magnetic separation,[3] magnetic hyperthermia,[4] and stem cell tracking.[5] However, the most researched application of MNPs in the biomedical field is as a contrast agent for MRI[6−9] which constitutes a powerful platform for the noninvasive real-time visualization of cancer-related, cardiovascular, liver, and neurodegenerative diseases.[6,10] This is mainly attributed to their low toxicity and strong T_2 performance,[6,11] the latter translating into dark contrast in the acquired MR images, which make MNPs promising candidates for use in the early diagnosis and monitoring of many human diseases.[12−14] The efficiency of a magnetic material as T_2 contrast agent is measured in terms of the transverse relaxivity (r_2); the higher the r_2, the more effective the T_2-MRI contrast agent.[15] This parameter is determined as the slope of the linear fitting of the inverse of the transverse relaxation time plotted against the concentration of the contrast agent,[8] representing the amount of contrast agent needed to reduce the transverse relaxation time by one second.

However, the successful performance of a magnetic material as MRI contrast agent is strongly related to its structural properties, namely, particle size and distribution, surface coating, and shape.[1] As a consequence, the saturation magnetization (M_S), colloidal stability, interaction with water molecules, and inhomogeneous induced magnetic field are also variables that affect the suitable performance of a contrast agent.[9,16,17] The effect of these variables on r_2 is generally described by the quantum-mechanical outer-sphere theory.[18,19]

When the size of the MNPs is within the motional average regime, which is the case of magnetic nanoparticles below the superparamagnetic limit, an increase of their particle size leads to an enhancement of the M_S, which in turn results in higher r_2 values.[8,15] The surface coating is another crucial factor that influences r_2. First, the surface coating can provide improved colloidal stability and biocompatibility to the NPs, both requirements for in vivo applications. Second, the molecules attached to the surface of the NPs can hinder water diffusion, or even immobilize nearby water molecules by hydrogen bonds.[17] This causes the water molecules to be more significantly influenced by the induced magnetic field, which affects the nuclear proton relaxation and consequently modifies r_2.[17] The way in which these coating molecules affect the r_2 is not completely understood on the basis of the existent theories, so more efforts are needed in order to elucidate the spin relaxation mechanisms of the water protons' nuclei that result from the interaction between the coating molecules and the surrounding water molecules.

Therefore, synthetic and functionalization steps play a key role in the performance of MRI contrast agents, allowing their physicochemical properties to be tailored by selecting a favorable methodology. Moreover, the desired implementation of MNPs in clinical setups will require the development of a simplified and fast process to prepare NPs with designed physicochemical properties.[20] The most common approach to synthesize MNPs with high crystallinity and narrow size distribution is by means of thermal decomposition procedures.[7] Nevertheless, the process is laborious and time-consuming (up to 2 days because of the preparation and purification requirements[20]) and requires the use of organic solvents and phase-transfer procedures (i.e., ligand exchange) to obtain MNPs with colloidal stability in aqueous media.[20] Therefore, it is desirable to develop a methodology to overcome these drawbacks of thermal decomposition while simultaneously generating NPs with excellent physical and chemical properties.

Sonochemistry has received increasing attention in recent years in materials science because of its ability to achieve unique hot spots with temperatures greater than 5000 K and pressures as high as 1000 atm.[21−23] Such conditions make this technique distinctive from other conventional methods and thus make this approach advantageous compared to the laborious thermal decomposition method. Sonochemistry has already been used to synthesize Fe_3O_4 NPs.[24−32] However, in most of the published papers, the synthesis time was still large (60−180 min).[26,28,30,31,33] Furthermore, although sonochemistry has already been used to functionalize MNPs, there is still a lack of information about its effects on the functionalization of Fe_3O_4 NPs and about broadening the number of nanoparticle coating candidates (this approach has been mainly used to coat Fe_3O_4 NPs with chitosan[33,34]).

Herein, we propose a new, straightforward, versatile, and fast methodology to produce functionalized Fe_3O_4 NPs with outstanding physicochemical properties and the potential to be applied as MRI contrast agents. It is important to emphasize that the proposed method provides Fe_3O_4 NPs in just 12 min and that the NPs show excellent magnetic properties, as well as colloidal stability and high r_2 values. A range of different coating agents (CAs) were used in this work [sodium poly acrylate (PAANa), trisodium citrate (CIT), sodium oleate (OLNa), and branched-polyethylenimine (BPEI)] to showcase the versatility of the approach. Moreover, several characterization techniques were employed to evaluate the structure and magnetic properties of the core, interaction between the coating agent and Fe_3O_4, and colloidal stability of the synthesized NPs in aqueous solutions. Finally, we demonstrated that the synthesized MNPs have a high potential to be applied as a MRI contrast agent. Therefore, our results represent a new prospect for obtaining superior-quality (mainly in terms of magnetic properties that govern performance in MRI) functionalized Fe_3O_4 NPs in a simple and rapid manner.

EXPERIMENTAL SECTION

Materials. Iron chloride (III) hexahydrate ($FeCl_3{\cdot}6H_2O$) and iron sulfate heptahydrate ($FeSO_4{\cdot}7H_2O$) were purchased from Vetec Química. PAANa (Mw = 5 100), BPEI (Mw = 10 000), CIT, and OLNa (82%) were purchased from Sigma-Aldrich. Ammonium hydroxide (29%) was purchased from Dinâmica Química. All of them were used without further purification.

Synthesis and Functionalization of Fe_3O_4 with PAANa, BPEI, and CIT. The synthesis and functionalization of Fe_3O_4 NPs were performed in a two-step synthesis, using an ultrasound probe (Ultrasonique Desruptor) with a frequency of 20 kHz and 585 W of power. The experimental setup is shown in Figure 1A. The structures of the CAs used in this work are presented in Figure 1B.

Initially, two water solutions were prepared, an iron salt solution (solution A) and a coating agent (CA) solution (solution B). Solution A contained 1.16 g (4 mmol) of $FeSO_4{\cdot}7H_2O$ and 1.85 g (7 mmol) of $FeCl_3{\cdot}6H_2O$ dissolved in 15 mL of deionized water. Solution B contained 1.0 g of CA in 4.0 mL of deionized water.

First, solution A was sonicated for 4 min until it reached a temperature of 60 °C. Then, 7.0 mL of concentrated NH_4OH was added (0.23 mL s^{-1}) under sonication using a buret. Thereafter, the color of solution A changed from orange to

DOI: 10.1021/acs.jpcc.7b04941
J. Phys. Chem. C 2017, 121, 24206−24222

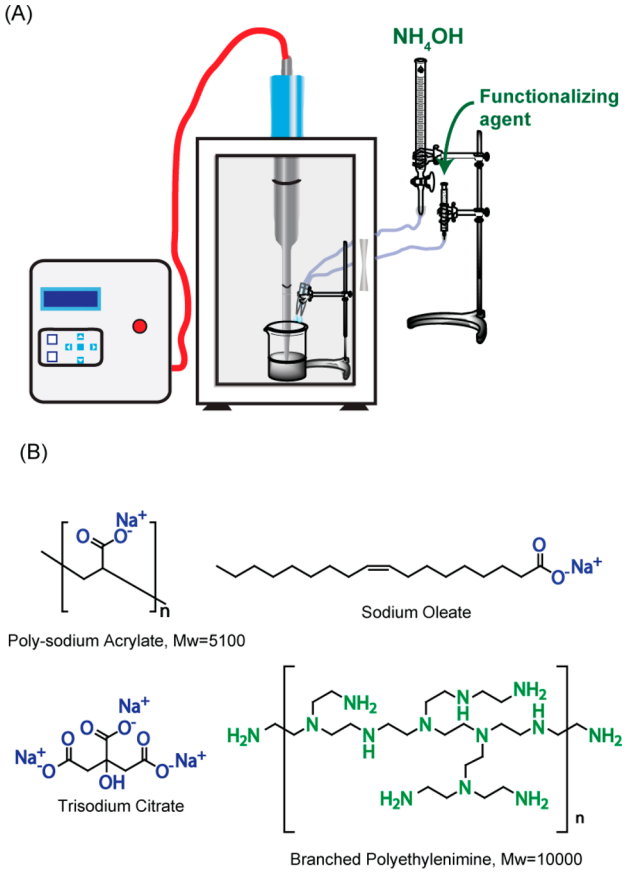

Figure 1. (A) Scheme of the experimental setup used in the synthesis and functionalization of MNPs. (B) Structure of CAs used in this work.

black, evidencing the formation of Fe_3O_4 NPs, and the reaction medium was sonicated for more 4 min. Finally, solution B was added (0.13 mL s^{-1}) to the reaction medium, which was kept under sonication for another 4 min. Thus, the ultrasound-assisted synthesis and functionalization of Fe_3O_4 NPs occurred in just 12 min.

To remove the excess NH_4OH and unbounded CA, the resultant NPs were washed several times with deionized water and precipitated with acetone. Finally, the NPs were dispersed in water and centrifuged for 10 min at 3000 rpm to remove large aggregates. The remaining functionalized NPs showed good colloidal stability in water. Thus, they were stored in deionized water and deaerated with argon to remove the dissolved oxygen. This procedure was used to generate three samples labeled as Fe_3O_4@PAANa, Fe_3O_4@BPEI, and Fe_3O_4@CIT.

Functionalization of Fe_3O_4 NPs with OLNa. The difference between this procedure and the former one is that the CA was dissolved with the iron salt solution. The reactant amounts remained the same. In this procedure, 1.0 g of OLNa was dissolved in 10.0 mL of deionized water at 60 °C. This solution was added to the iron salt solution (solution A) and sonicated for 4 min, reaching a maximum temperature of 60 °C. Then, 7.0 mL of concentrated NH4OH was added under sonication, and the reaction medium was sonicated for an additional 8 min. The NPs dispersion was washed with distilled water to remove the excess NH_4OH. Afterward, *n*-hexane and ethanol were used to purify the hydrophobic coated NPs by removing the unbounded OLNa molecules. Finally, the NPs were dispersed in hexane and centrifuged for 10 min at 3000 rpm to remove large aggregates. The NPs were stored in cyclohexane, and the ferrofluid generated in this procedure was labeled as Fe_3O_4@OLNa.

In both experimental procedures, the amount of materials produced is approximately 800 mg per batch.

Characterization of the NPs. The core structure of the obtained NPs was evaluated by X-ray diffraction (XRD) using an X'Pert MPD X-ray powder diffractometer (PANalytical, Westborough, United States) with 40 kV and 30 mA in a scanning range of 2θ = 20−80°. A Cu Kα tube was used for the Fe_3O_4@PAANa, Fe_3O_4@BPEI, and Fe_3O_4@OLNa samples, while a Co Kα tube was used in the analysis of the Fe_3O_4@CIT sample. The diffraction patterns were obtained using a Bragg−Brentano geometry in the continuous mode with a speed of 0.5°/min and step size of 0.02° (2θ). The Rietveld structure refinement was used to interpret and analyze the diffraction data using the program DBWstools 2.4.[35] The full-width at half-maximum (fwhm) of the instrument was calculated with the standard hexaboride lanthanum. The crystallite size of each sample was calculated using Scherrer's equation.

A transmission electron microscopy (TEM) analysis of the synthesized nanoparticles was performed using a JEOL JEM 1011 (JEOL, Tokyo, Japan) operating at 100 kV and equipped with a CCD camera (Gatan Orius 831). A drop of each aqueous NP dispersion was deposited onto a carbon-coated Cu grid. Subsequently, the specimens were dried overnight before being analyzed. The size distribution curves were obtained by manually measuring the sizes of 200 particles,[36] using the software ImageJ (U.S. National Institutes of Health, Bethesda, MD). The polydispersity index for the TEM analysis (PDI_{TEM}) was calculated as reported in the literature.[37]

The Mössbauer spectroscopy (MS) data were recorded at room temperature (300 K) with a FAST (ConTec) Mössbauer system spectrometer using the transmission geometry. A ^{57}Co radioactive source was used. The data analysis was performed using the NORMOS program written by R. A. Brand (distributed by Wissenschaftliche Elektronik GmbH, Germany). The isomer shifts (d) relative to α-Fe were found at room temperature.

Magnetic measurements were carried out on powder samples using a superconducting quantum interference device SQUID-VSM magnetometer from Quantum Design. Prior to the measurements, the particles were dried overnight in vacuum at room temperature, ground using an agate mortar, and finally placed in gelatin capsules for the measurements. Hysteresis loops were obtained at 300 K by applying a magnetic field up to ±20 kOe. Magnetic curves as a function of the temperature were also recorded in zero-field-cooled and field-cooled (ZFC-FC) conditions at a fixed applied field of 100 Oe in the temperature range of 2−300 K.

The presence of the CAs on the surface of the NPs was confirmed by Fourier transform infrared spectroscopy (FTIR). The samples were ground in an agate mortar and pressed into discs of KBr at a mass ratio of 1:10 (sample:KBr). The spectra were recorded in vacuum to avoid interference from water and carbon dioxide using a Vertex 70v. The range used was 4000−400 cm^{-1}, with a resolution of 2 cm^{-1} and 128 scans.

The amount of CA molecules and how they were organized on the surface of the NPs were evaluated using thermogravimetric analysis (TGA). The measurements were performed using a Mettler Toledo TGA/simultaneous differential thermal analysis (TGA/SDTA) 851e machine. A nitrogen atmosphere

DOI: 10.1021/acs.jpcc.7b04941
J. Phys. Chem. C 2017, 121, 24206−24222

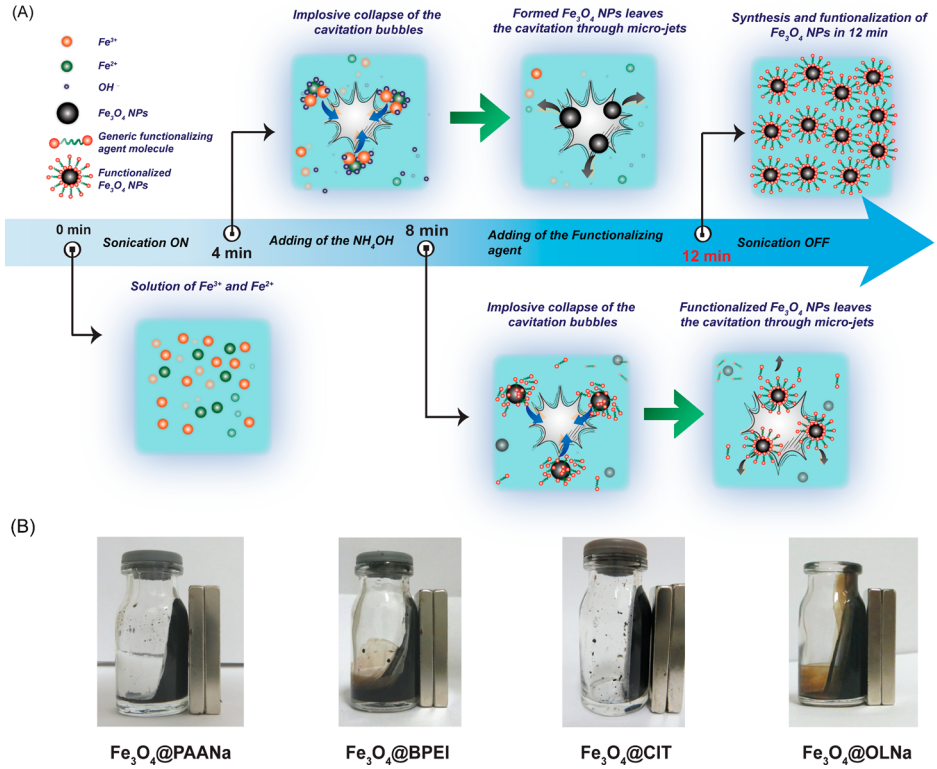

Figure 2. (A) Timeline of the synthesis and functionalization of MNPs during a sonochemical reaction and proposed mechanism. (B) Magneto-fluid response of the samples herein synthesized.

was used (50 cm^3/min), with a heating rate of 10 °C/min between 25 and 800 °C and a sample mass of 10 mg. The previously method reported in the literature was used for the quantitative analysis of the amount of grafted CA molecules.[38]

The hydrodynamic size of the NPs in solution was measured in DLS experiments using a Malvern zetasizer NS 3601 at 25 °C. The DLS measurements were performed on a diluted solution of the NPs (0.066 mg/mL), with a single scattering angle of 173°. The hydrodynamic size of the synthesized samples was further analyzed using phosphate buffers at pH 7.4 (PB 7.4) and PB at different salt concentration (PBS 7.4), as previously reported.[39] The DLS size of the samples was expressed as *Z*-average values, and the polydispersity index (PDI_{DLS}) values were calculated using the cumulate method. Five measurements were performed for each sample. The surface zeta potential (ζ) of each sample was measured using the same instrument at 25 °C. The ζ value was also measured using PB 7.4 as solvent.

Relaxivity Measurements and MRI-Weighted Images. Four aqueous dilutions with different nanoparticle concentrations (between 0 and 0.25 mM Fe) were prepared for each sample. The 200 μL samples of each dilution were measured in a minispec mq60 contrast agent analyzer from Bruker at 37 °C and under 1.41 T magnetic field, with standard inversion recovery sequence for T_1 and Carr Purcell Meiboom Gill (CPMG) for T_2 calculations. The relaxivity constants (r_1 and r_2) were calculated as the slope of the curve obtained by fitting the T_1^{-1} or T_2^{-1} values versus the Fe concentration (mM). The Fe concentrations of the solutions were calculated using an inductively coupled plasma-optical emission spectroscopy (ICP-OES) analyzer (Shimadzu ICPE-9000).

MR phantom imaging was performed in a 3 T horizontal bore MR Solutions Benchtop (Guildford, U.K.) equipped with 48 G cm^{-1} actively shielded gradients. For imaging the sample, a 56 mm diameter quadrature bird-cage coil was used in transmit/receive mode. For the phantom measurements, the samples at different concentrations (between 25 and 500 μM in Fe) were dissolved in 200 μL of Milli-Q water in 300 μL tubes. All MR images of the phantoms were acquired with an image matrix 256 × 252, field of view (FOV) 60 × 60 mm, three slices with a slice thickness of 1 mm, and 1 mm slice gap. For T_2-weighted imaging a fast spin echo (FSE) sequence with the following parameters was used: T_E = 68 ms, T_R = 4800 ms, N_A = 50. For T_1-weighted imaging, a FSE sequence with T_E = 11 ms, T_R = 400 ms, and N_A = 50 was used. Postprocessing was performed using ImageJ software (Rasband, W. NIH).

RESULTS AND DISCUSSION

Synthesis and Magneto-fluid Response. Sonochemistry has been proven to be a powerful tool for preparing a wide range of materials.[21,22] The interesting feature of this methodology is that under ultrasound irradiation, the alternating acoustic waves create bubbles in an oscillating manner. These bubbles grow to a certain size and then collapse, releasing a concentrated burst of energy within a short time. The energy is so localized that the collapsing bubbles can quickly increase the temperature up to 5000 K and reach pressures as large as 1000 bar.[22,40,41] These conditions are capable of speeding up chemical reactions.[42] We believe that these events occurred during the synthesis and functionalization steps of the NPs reported here. Figure 2A summarizes the timeline of all the events that occur during a typical sonochemical reaction and the possible physical mechanisms underlying the experimental stages involved in the NPs synthesis and functionalization. A similar mechanism based on the implosion collapse of cavitation bubbles has been also

DOI: 10.1021/acs.jpcc.7b04941
J. Phys. Chem. C 2017, 121, 24206−24222

proposed for the sonochemical synthesis of hydroxyapatite NPs,[43−45] although in this case the sonochemistry approach was also used to functionalize the surface of Fe_3O_4 NPs with a wide range of CAs (Figure 2A).

During the first 4 min of the synthesis, a mixture of Fe^{2+} and Fe^{3+} was sonicated to reach a temperature of ∼60 °C, after which concentrated NH_4OH was added to the reaction medium. Then, ferrous, ferric, and hydroxide ions were adsorbed on the cavitation bubbles, followed by their implosive collapse. This event induced a collision between the ions at high temperatures and pressures, which subsequently led to the formation of Fe_3O_4 NPs (Figure 2A). The reaction medium was kept under sonication for 4 min more to allow the particles to grow to the desired size and crystallinity. At this time, the selected CA was added, and the reaction was left under sonication for an additional 4 min, which produced CA-functionalized Fe_3O_4 NPs (see Figure 2A).

It is well-known that the presence of a CA during the nucleation of the Fe_3O_4 NPs hinders the NP growth and crystallization of MNPs, resulting in low M_s.[46] In our sonochemical approach, the hydrophilic CAs (PAANa, CIT, and BPEI) are added to the reaction after NH_4OH addition. At this stage, the high energy at the cavities allows the MNPs to interact efficiently with the CAs, yielding colloidal water-stable nanoparticle dispersions, as evidenced by the magneto-fluid response of the prepared NPs (Figure 2B). Thus, this strategy made it possible to obtain NPs with excellent magnetic properties and colloidal stability in aqueous solvents, which are key requirements for biological applications.

Structural and Magnetic Characterizations. *XRD.* The lattice structure and phase composition of the MNPs were evaluated using XRD combined with Rietveld structural refinement. The diffraction patterns of the prepared samples are shown in Figure 3. A Rietveld analysis was performed to acquire deeper information about the crystal structure of the synthesized MNPs. These results are summarized in Table 1. Both the percentage of errors (R_{WP}) and goodness of fitting (S) values were found to be in agreement with those of a high-quality refinement.[47]

The analysis of the position and intensity of the XRD reflections indicated that the core structures of the NPs were composed of a cubic inverse spinel structure *Fd*3*m* (ICSD code: 84611),[48] which is characteristic of Fe_3O_4. However, the diffractograms also assign the oxidized phase (maghemite, γ-Fe_2O_3). Although the two phases exhibit similar XRD patterns, the calculated cubic cell lattice parameter (a) can provide insight concerning the oxidation of Fe_3O_4 NPs: the a value for Fe_3O_4 is 8.396 Å (JCPDS file 19-629), while for γ-Fe_2O_3 (JCPDS file 39-1346) the value is 8.346 Å. Therefore, an a intermediate value between two phases indicates the presence of Fe_3O_4 and γ-Fe_2O_3.[49,50] For our samples, a values are shown in Table 1, and their intermediate values denote an oxidized Fe_3O_4, which is expected, because the oxidation of the NPs increases as the size of the NPs decreases below 20 nm. Indeed, Salazar et al. reported that below 20 nm single Fe_3O_4 NPs are nonstoichiometric in their whole volume and cannot be assigned as magnetite.[51]

In accordance, this behavior is also observed when the oxidation of Fe^{2+} takes place at the surface of Fe_3O_4, in which a vacancy (δ) occupies the octahedral sites, generating a nonstoichiometric Fe_3O_4 that is expressed in a $Fe_{3-\delta}O_4$-form.[51,52] On the other hand, we cannot exclude other sources for the formation of vacancies. For instance, Kolen'ko et al.

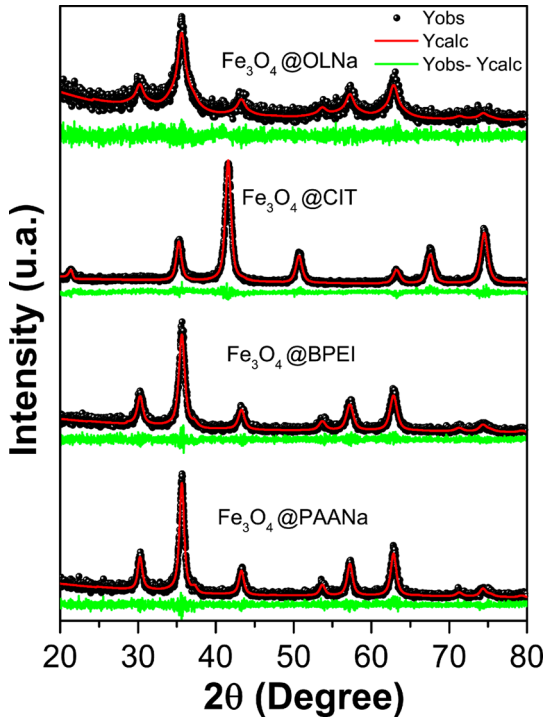

Figure 3. XRD patterns of the as-synthesized NPs. The black dots and red line show the experimental and calculated data, respectively. The green line represents the difference between the experimental and the calculated data.

prepared PAANa-coated MNPs with a values close to that of γ-Fe_2O_3. However, Raman and X-ray photoelectron spectroscopy evidenced a minor admixture of the γ-Fe_2O_3 phase.[53] Additionally, Lu et al. found that the CA slightly influences the a cell parameter in functionalized MNPs.[54] Moreover, some authors reported that the increasing of a values with size decreases for Fe_3O_4 NPs.[55,56] Therefore, we believe that the oxidation of Fe_3O_4 was not the only source for δ in our samples, mainly based on the high obtained M_S values, once oxidation of Fe_3O_4 leads to a decreasing of magnetization.

The narrow and well-defined peaks evidenced a high crystallinity and small crystallite sizes for all the functionalized samples. Only the Fe_3O_4@OLNa showed a significant lower average crystallite size compared to the rest of functionalized MNPs. This could be due to the addition of the CA to the reaction medium before the precipitation of the nanoparticles. The presence of carboxylate groups in OLNa molecules is able to strongly chelate the Fe ions in solution, thus hindering the growth of the MNPs and leading to smaller and not so well crystallized nanoparticles.[46] Furthermore, the crystallite sizes obtained by the Scherrer's equation (considering all the reflections of the XRD pattern) were in good agreement with the average particle size determined from the TEM images in all the samples, as shown in Table 1 and Figure 4A−D. Results also showed that there is not any systematic effect of the CA on the crystallite size or the particle size of the MNPs in any of the samples Fe_3O_4@CIT, Fe_3O_4@BPEI, and Fe_3O_4@PAANa. However, the slight decrease in both crystalline size and average particle size observed in Fe_3O_4@OLNa could confirm the growth inhibition that these particles experience when the CA is added to the reaction prior to the particles' precipitation.

TEM. The morphology and structure of the MNPs were evaluated using TEM. The micrographs and particle size

DOI: 10.1021/acs.jpcc.7b04941
J. Phys. Chem. C 2017, 121, 24206−24222

Table 1. Structural Parameters Extracted from XRD Patterns (through Rietveld Refinement) and TEM Analysis

	XRD				TEM	
sample	lattice parameters (a) (Å)	R_{wp} (%)	S	average crystallite size (nm)	average particle size (nm)	PDI_{TEM}
Fe_3O_4@OLNa	8.362	15.48	0.89	7.0 ± 0.1	8 ± 3	0.416
Fe_3O_4@CIT	8.360	13.75	1.01	12.9 ± 0.2	11 ± 3	0.256
Fe_3O_4@BPEI	8.374	15.18	0.89	10.2 ± 0.2	10 ± 3	0.280
Fe_3O_4@PAANa	8.372	15.41	0.87	12.7 ± 0.2	11 ± 3	0.293

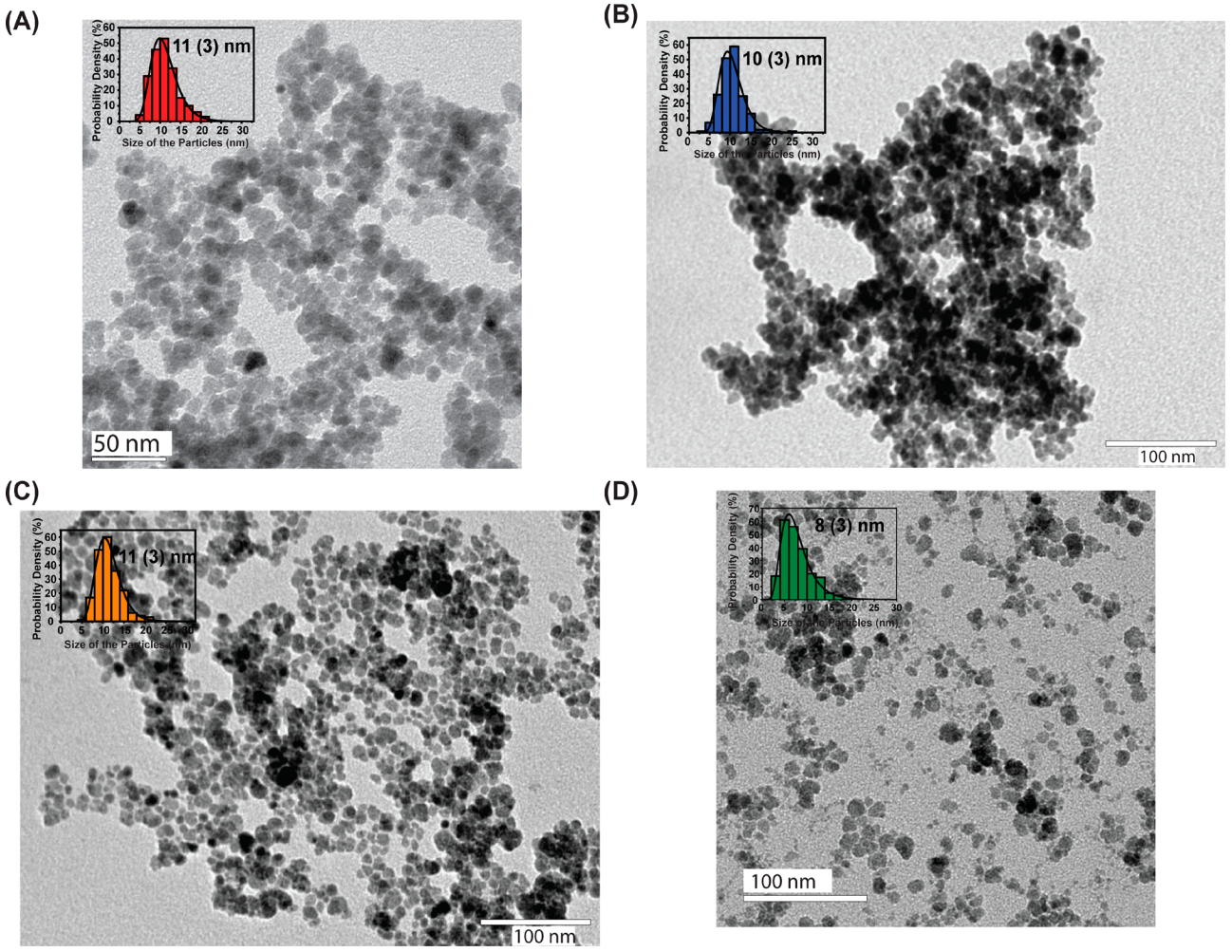

Figure 4. TEM micrographs and particle size-distribution curves of the samples (A) Fe_3O_4@PAANa, (B) Fe_3O_4@BPEI, (C) Fe_3O_4@CIT, and (D) Fe_3O_4@OLNa.

distribution curves of the Fe_3O_4@PAANa, Fe_3O_4@BPEI, Fe_3O_4@CIT, and Fe_3O_4@OLNa samples are shown in Figure 4A–D. Additionally, the average particle diameters are listed in Table 1. TEM micrographs showed that the synthesized NPs possess a spherelike morphology, which is expected when the preparation of Fe_3O_4 NPs is performed through the coprecipitation of the Fe^{2+} and Fe^{3+} ions with ammonium hydroxide.[53,57] Furthermore, the sonochemistry approach proposed in this work produced monodisperse NPs with a narrow particle size distribution, as evidenced by the PDI_{TEM} values (Table 1). This characteristic is particularly significant for their use in the biomedical field.[58] For the sample Fe_3O_4@OLNa, the average diameter calculated by TEM was smaller than that of the other samples, although statistically the average size of all samples is similar. However, the higher PDI_{TEM} for Fe_3O_4@OLNa demonstrates that this sample has heterogeneity in core size, which explains the smaller size obtained by XRD, and the different profile observed in MS and magnetic measurements, because the degree of dipolar interactions decreases as the core size decreases.[59] This behavior was already explained in the XRD discussion.

Mössbauer Spectroscopy. MS has been extensively used to study iron-containing materials because the MS spectrum contains information about the structural, electronic, and magnetic properties of the studied material.[60] The MS spectra of all the samples are shown in Figure 5A. Fe_3O_4@PAANa, Fe_3O_4@BPEI, and Fe_3O_4@CIT samples showed broadened ferrimagnetic sextets. Therefore, a magnetic hyperfine field distribution was used to fit the measured spectra. This distribution is shown in Figure 5B. On the other hand, the Fe_3O_4@OLNa sample showed a well-resolved paramagnetic doublet in addition to a ferrimagnetic sextet. Thus, a model

DOI: 10.1021/acs.jpcc.7b04941
J. Phys. Chem. C 2017, 121, 24206–24222

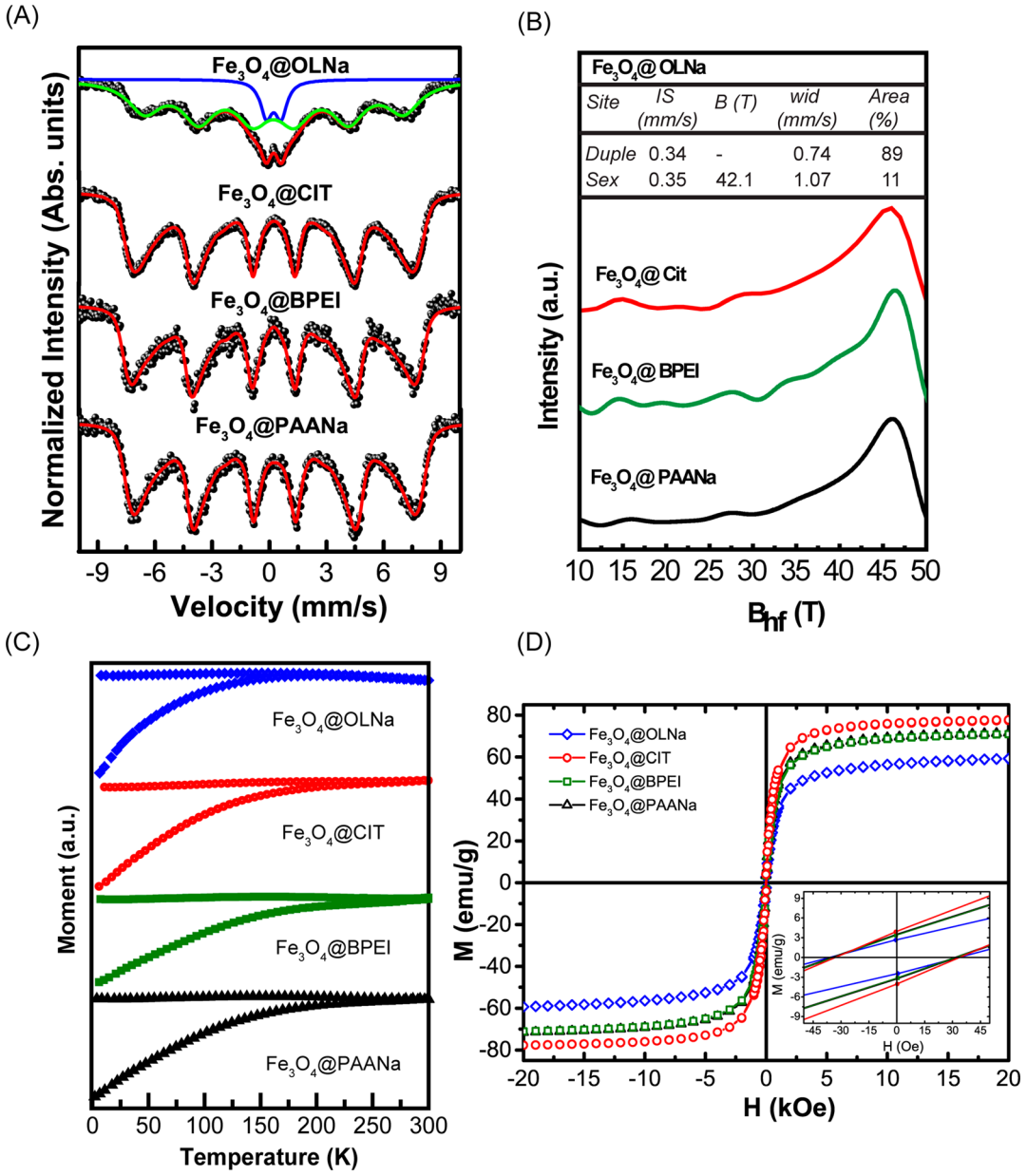

Figure 5. (A) MS spectra of the as-synthesized samples. The black dots and red lines represent the experimental and calculated data, respectively. For the Fe_3O_4@OLNa sample, the green and blue lines are the site distributions for the populations of NPs under ferri- and superparamagnetic regimes, respectively. (B) Hyperfine field distribution curves of each sample. The table at the top of the image summarizes the data extracted from the site distribution: duple, doublet; sex, sextet; IS, isomer shift; *B*, magnetic hyperfine field; wid, line width. (C) ZFC and FC magnetization curves and (D) hysteresis loops of the as-synthesized samples. Inset is a zoom of the low-field region.

with two crystalline sites was used to fit the spectrum (Figure 5A,B).

First, it is important to mention that the MS spectrum of the bulk Fe_3O_4 at room temperature is composed of two well-resolved ferri- or ferromagnetic sextets, which corresponded to Fe^{3+} in tetrahedral sites and Fe^{3+} and Fe^{2+} on octahedral sites. As the size of the particles decreases, the sextets exhibit broadened lines as a result of the presence of superparamagnetic fluctuations.[61] A further decrease in the size of the particles leads to a change in the MS spectrum. Specifically, the broad sextet becomes a paramagnetic doublet, which is characteristic of superparamagnetic NPs.[62] This critical size for Fe_3O_4 is around 25−30 nm.[53] Therefore, a doublet in MS spectra for the samples would be expected, once their average diameters are below this critical size, as observed by XRD and TEM. However, when MNPs exhibit dipolar interactions, they present broadened sextets even for NPs below the superparamagnetic critical size,[63,64] which is noticed for the samples Fe_3O_4@PAANa, Fe_3O_4@BPEI, and Fe_3O_4@CIT. This assumption is supported by ZFC-FC results (see the magnetic measurements discussion). Moreover, the profiles of the spectra of these particles were similar to those reported in the literature for 8−20 nm Fe_3O_4 NPs.[53,60,63]

Conversely, because of the clear presence of a doublet in the MS spectrum of Fe_3O_4@OLNa, it is possible to assert that these NPs are less interacting than the others (Figure 5A,B). This was corroborated by the area of the calculated doublet (89%), which was greater than that of the sextet (11%), as shown in the top region of Figure 5B. The sextet can be assigned to supra-structures assembled by dipolar interac-

DOI: 10.1021/acs.jpcc.7b04941
J. Phys. Chem. C 2017, 121, 24206−24222

tions.[65] Pauly et al. and Fleutot et al. reported that decreasing of the size and interparticle distance lead to a decrease of dipolar interactions in MNPs.[59,66] Thus, we believe that these facts explain the different profiles of MS spectra of Fe_3O_4@OLNa: the smaller size showed by XRD and TEM analysis due to nucleated and grew chelated particles with OLNa molecules led to an increase in interparticle distance. Indeed, TEM images show that Fe_3O_4@OLNa does not exhibit as many larger aggregates as the other samples (Figure 4A−D). The calculated hyperfine parameters included the isomer shift (IS) and line width of the doublet, which had values of 0.34 and 0.74 mm/s, respectively, along with those for the sextet, which were determined to be 0.35 and 1.07 mm/s, respectively. In addition, the hyperfine field for the sextet was found to be 42.1 T. These values were in agreement with those for the 6 nm for Fe_3O_4 NPs reported by Mikhaylova et al.[67]

Furthermore, the MS can also give information concerning the oxidation degree of Fe_3O_4, mainly through the average IS, once this parameter is driven by the electrostatic environment of Fe nucleus, which includes atomic charge state (Fe^{2+} or Fe^{3+}) and local oxygen coordination.[68] The average IS for our NPs were calculated through magnetic hyperfine field distribution adjustment, and the values are 0.334 ± 0.005, 0.327 ± 0.008, 0.328 ± 0.003, and 0.341 ± 0.06 mm/s for the samples Fe_3O_4@PAANa, Fe_3O_4@BPEI, Fe_3O_4@CIT, and Fe_3O_4@OLNa, respectively. To keep the same method of the calculation, the average IS for Fe_3O_4@OLNa was obtained also by magnetic hyperfine field distribution fitting. The IS values of our samples are close to the value of γ-Fe_2O_3 (0.32 mm/s), which indicates that our NPs are constituted of partially oxidized and nonstoichiometric Fe_3O_4. Indeed, Salazar et al. prepared MNPs with 10−40 nm and noticed by MS that below 20 nm these MNPs have vacancies in their whole volume and cannot be assigned as Fe_3O_4.[51] The created vacancies are due to oxidation of Fe^{2+} that likely occurred during the synthesis or under exposure to air. However, existence of just γ-Fe_2O_3 in our samples is not supported by XRD, FT-IR, and VSM. First, the M_S values of the prepared samples are close to (PAANa- and BPEI-coated NPs) or higher than (CIT-coated NPs) the value for γ-Fe_2O_3 bulk (76 emu/g). Thus, the existence of just γ-Fe_2O_3 would be reasonable unless no spin canting was present in the synthesized NPs, which contradicts the results of Baaziz et al. which report volume and surface spin canting in MNPs within the range of 8−12 nm.[50] Additionally, a (XRD) values and wavenumber for stretching of Fe−O bond (FT-IR) present intermediate values between Fe_3O_4 and γ-Fe_2O_3, as shown in the XRD and FT-IR discussion. Therefore, these low values of average IS for our samples are probably due to additional coordination environments of Fe atoms, which are characteristic of Fe_3O_4/γ-Fe_2O_3 NPs, as observed with the presence of several peaks in magnetic hyperfine distribution (Figure 5B) and also reported in the literature.[69−72] Moreover, some reports evidenced that the presence of CA affects the average IS values.[71,73,74]

There is no agreement in the literature concerning the model which describes the structure and composition of non-stoichiometric Fe_3O_4 NPs in the size range of 8−20 nm. To the best of our knowledge, there are four models: distinct core−shell-like structure, such as Fe_3O_4@γ-Fe_2O_3;[55] individual particles, implying that when the oxidation starts it occurs throughout the entire particle volume;[75] oxidation gradient from the surface to the center of the nanoparticles, which generates nonstoichiometric NPs in their entire volume;[51] and Fe_3O_4-γ-Fe_2O_3 solid solution with excess of Fe^{3+} distributed along the NPs, with possible enrichment at their surfaces.[76] Indeed, the two latter models are similar. Thus, based on structural and magnetic characterization presented in this paper, which evidenced nonstoichiometric and oxidized Fe_3O_4 NPs, and the similarity of our NPs with the ones prepared in the reports of Kolen'ko et al.,[53,76] we hypothesize that the NPs synthesized herein are best understood as Fe_3O_4−γ-Fe_2O_3 solid solution with an excess of Fe^{3+} (structural defects) distributed in their entire volume. However, this does not exclude the presence of oxidation gradient in our NPs. In order to evidence this, surface-sensitive measurements would be performed for our samples.

Magnetic Measurements. The magnetization curves as a function of the temperature were measured under ZFC-FC conditions for all the as-synthesized samples (Figure 5C). Evidence of a strong magnetic dipolar particle interaction can be observed for all samples in the flat profile of the FC curves at low temperatures.[53] The ZFC curves for the samples Fe_3O_4@PAANa, Fe_3O_4@BPEI, and Fe_3O_4@CIT did not show any maximum in the range of temperature measured, indicating that the superparamagnetic blocking temperatures (T_B) for these samples are above 300 K.[53] However, the sample Fe_3O_4@OLNa showed a T_B at 196 K, which corresponded to the maximum of the ZFC curve. The T_B value below 300 K for Fe_3O_4@OLNa indicates that this sample has a lower degree of dipolar interactions, once the weaker the strength of dipolar interaction, the lower the T_B.[77] This result is also supported by XRD, TEM, and mainly MS results, in which a paramagnetic doublet was evidenced for this sample (Figure 5A,B). Actually, this different behavior was already explained in the MS discussion. In summary, ZFC-FC results indicate that all synthesized NPs herein present strong dipolar interactions (which are significantly weaker for Fe_3O_4@OLNa) due to the presence of aggregates that may have been formed and then functionalized.

The hysteresis loops of the as-synthesized samples at 300 K are shown in Figure 5D. The low-field regions of the curves are shown in the insets, which reveal small hysteresis loops. These data allowed for the calculation of the M_s, remanent magnetization (M_r), and coercivity (H_C) values, which are summarized in Table 2.

Table 2. Magnetic Parameters Extracted from the Experimental Magnetic Data of the As-Synthesized Functionalized Samples

sample	M_s (emu/g)	M_r (emu/g)	H_C (Oe)
Fe_3O_4@OLNa	59.27	2.70	34.27
Fe_3O_4@CIT	77.36	3.96	33.90
Fe_3O_4@BPEI	70.98	3.43	33.21
Fe_3O_4@PAANa	71.51	3.45	35.26

Interestingly, the H_C values for all the samples were very similar even for the Fe_3O_4@OLNa sample, which showed a T_B significantly below room temperature, duplet in the MS spectra, and smaller mean particle diameter compared to the other synthesized samples. This is assumed to be due to electric currents trapped in the superconducting coil of the squid magnetometer, which induce artificial broadenings of the hysteresis loops up to 20 Oe for all the samples (see inset in Figure 5D).

DOI: 10.1021/acs.jpcc.7b04941
J. Phys. Chem. C 2017, 121, 24206−24222

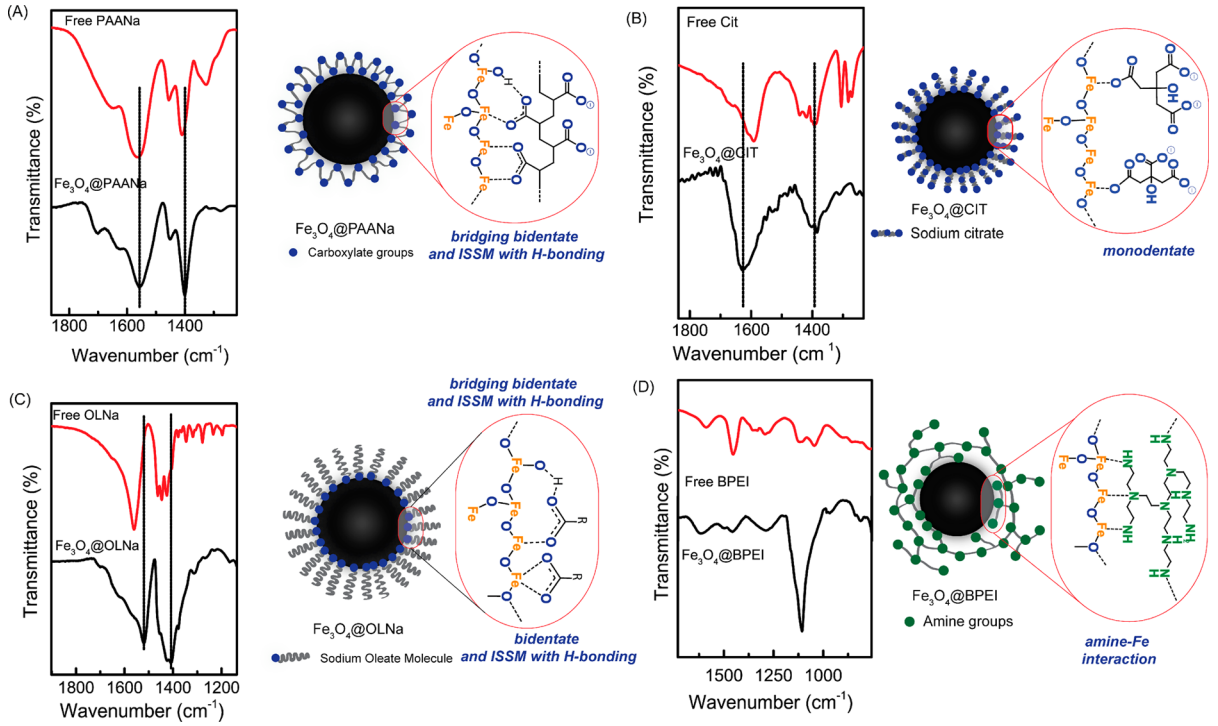

Figure 6. FT-IR spectra for the as-synthesized coated MNPs (left) and model of the interactions between the CA molecules and Fe ions of MNPs (right) for the samples (A) Fe_3O_4@PAANa, (B) Fe_3O_4@CIT, (C) Fe_3O_4@OLNa, and (D) Fe_3O_4@BPEI. For each sample, the spectra of the functionalized NPs and free CAs molecules are shown.

Clearly the M_s values for all the samples were smaller than the bulk value of Fe_3O_4 (~98 emu/g).[53] This was due to the existence of a surface spin disorder layer as the particle size decreases, which substantially decreases the M_s of nanoparticles below 20 nm.[78] Our samples certainly possessed large M_s values relative to other functionalized or nonfunctionalized Fe_3O_4 NPs with comparable or larger core sizes synthesized using different protocols.[58,79−82] For instance, Wu et al. obtained ~11 nm CIT-coated Fe_3O_4 NPs with a M_s value of 52 emu/g using a hydrothermal method.[58] Also, Calatayud et al. used an oxidative hydrolysis method to prepare PAANa- and BPEI-coated Fe_3O_4 NPs with diameters of 32 and 25 nm, respectively, and M_s values of 54.0 and 51.0 emu/g, respectively.[80] Furthermore, our samples showed M_s values higher than the ones obtained by coprecipitation method.[83−89] For instance, Gupta et al. synthesized PAANa coated Fe_3O_4 NPs with average diameter around 8−10 nm, under a temperature at 90 °C with a total synthesis time of 3h and M_s of 56 emu/g.[85] Similarly, Nigam et. al obtained CIT functionalized Fe_3O_4 NPs around 2h with the same average diameter and temperature, leading to MNPs with M_s of 57 emu/g.[87] We believe that the major contribution to the remarkable enhancement of M_s comes from the ultrasonic irradiation used in the synthesis of the NPs. As previously mentioned, the implosive collapse of the cavitation bubbles generates high energy levels, which increases the reaction rates, leading to NPs with higher crystallinity and consequently greater M_s values. Furthermore, the mentioned high energy during the synthesis induced a greater rate of functionalization of NPs, which reduced the magnetic dead layer by binding the Fe atoms at the surface.[90] It is worth mentioning that one of the problems with surface coated MNPs is the reduction of their magnetization due to the presence of a considerable relative amount of nonmagnetic compounds,[20] an issue that was overcome using the methodology proposed in this work to obtain coated NPs with excellent magnetic properties.

Coating. In this work, FTIR and TGA were used to study the passivating layer of the functionalized NPs. FTIR was used to evaluate the effectiveness of the sonochemistry approach in functionalizing Fe_3O_4 with PAANa, CIT, BPEI, and OLNa, and TGA was used to determine the amount of mass of CA present on the Fe_3O_4 NP surface.

FTIR. Figure 6A−D (left) shows the FTIR spectra of the functionalized samples and free CA molecules. For the sake of clarity, only the wavenumber range of interest is presented. The full spectra of the functionalized samples, free CAs, and nonfunctionalized Fe_3O_4 can be found in Figure S1. All of the functionalized samples revealed two bands between 400 and 800 cm^{-1} (Figure S1) attributed to the stretching of the Fe−O (ν_{Fe-O}) bond in tetrahedral and octahedral sites.[48] These vibrational modes are highlighted in Figure S2; they can also provide information concerning the composition of MNPs in terms of Fe_3O_4/γ-Fe_2O_3.[91] This differentiation comes from the fact that ν_{Fe-O} for Fe_3O_4 consists of a broad band located between 580 and 590 cm^{-1} with a shoulder at 700 cm^{-1} due to the oxidized surface, whereas γ-Fe_2O_3 displays several bands between 800 and 400 cm^{-1}.[50] Thus, the position of the maximum of ν_{Fe-O} with intermediate values between Fe_3O_4 (571 cm^{-1}) and γ-Fe_2O_3 (638 cm^{-1}) pointed to partially oxidized NPs.[50] The maximum of ν_{Fe-O} for the samples Fe_3O_4@PAANa, Fe_3O_4@BPEI, Fe_3O_4@CIT, and Fe_3O_4@OLNa were 581, 579, 583, and 606 cm^{-1}, respectively, indicating that the synthesized NPs consist of partially oxidized Fe_3O_4, as evidenced in XRD and MS analysis.

Regardless of the type of ligand, in the case of PAANa, CIT, and OLNa, the anchoring of the CA onto the magnetic core occurred through carboxylate groups. Therefore, the spectra of these three samples mainly show two vibrational modes in the

DOI: 10.1021/acs.jpcc.7b04941
J. Phys. Chem. C 2017, 121, 24206−24222

Table 3. Hydrodynamic Particle Sizes and Surface Charge Obtained by DLS in Different Aqueous Solvents

sample	solvent	Z-average size (nm)	PDI	ζ (mV)
Fe_3O_4@PAANa	H_2O	89.4 ± 1.1	0.079 ± 0.030	−55.5 ± 8.6
	PB 7.4	131.7 ± 0.6	0.072 ± 0.003	−30.6 ± 1.8
	PBS 7.4	117.8 ± 0.2	0.111 ± 0.028	–
Fe_3O_4@BPEI	H_2O	109.1 ± 5.0	0.060 ± 0.018	+44.5 ± 6.0
Fe_3O_4@CIT	H_2O	120.2 ± 1.0	0.094 ± 0.010	−32.4 ± 0.8
	PB 7.4	119.6 ± 0.9	0.106 ± 0.010	−41.7 ± 4.2

regions of 1300−1500 cm^{-1} and 1550−1700 cm^{-1}, which are related to the symmetric (ν_{syCO}) and asymmetric (ν_{assyCO}) C−O stretching modes, respectively (Figure 6A−C, left). Moreover, the wavenumbers of these bands changed after the functionalization as a result of the interaction with the Fe_3O_4 surface.[92] The carboxylic acid (or carboxylate) groups can bind oxide surfaces through "outer-sphere interaction" and/or "inner-sphere interaction".[93] In the first case, this interaction occurred through the H-bond with the −OH groups present on the surface of the oxides.[93] In contrast, in the second case, the interaction took place via coordination bonds between the metal and −COOH (or carboxylate) groups.[93]

Traditionally, the splitting ($\Delta_{\nu CO}$) between the ν_{SyCO} and ν_{assyCO} vibrational modes is employed to specify the interaction configuration of carboxylate groups in surface oxides.[92,94] This method states that monodentate binding occurs if $\Delta_{\nu CO} > 200$ cm^{-1}, whereas bidentate binding occurs when $\Delta_{\nu CO} < 110$ cm^{-1}, and a bridging bidentate better describes the carboxylate−metal coordination when $140 < \Delta_{\nu CO} < 200$ cm^{-1}.[94,95] This approach is based on the $\Delta_{\nu CO}$ values for the bulk of several coordination compounds, the structures of which were confirmed by XRD.[96] Hence, an extrapolation must be performed to apply this approach to functionalized NPs. However, in the work of Lens et al., the $\Delta_{\nu CO}$ correlation approach agreed with quantum-chemical calculations for the functionalization of ZnO NPs.[97] For our samples, the $\Delta_{\nu CO}$ values were 158, 243, and 97 cm^{-1} for Fe_3O_4@PAANa, Fe_3O_4@CIT, and Fe_3O_4@OLNa, respectively. These values indicated that the types of interaction in the synthesized samples were the bridging bidentate, monodentate, and bidentate, respectively, as illustrated in Figure 6A−C (right).

However, Chernyshova et al. performed a comprehensive spectroscopic and theoretical study that found numerous drawbacks for the $\Delta_{\nu CO}$ correlation approach.[98] The authors reported that fatty acids adsorb onto iron oxides as a mixture of an inner-sphere monodentate mononuclear (ISMM) complex with H-bonded second carboxylate oxygen and an outer-sphere complex (OS hydration-shared complex). A fact that we can correlate with our results is the authors' attribution of a shoulder below 1720 cm^{-1} and above 1696 cm^{-1} to an ISSM complex with H-bonded second carboxylate oxygen (C═O···· H). This band is seen in the Fe_3O_4@PAANa and Fe_3O_4@OLNa samples at 1706 and 1702 cm^{-1}, respectively.

In summary, on the basis of our FTIR results, we deduce that the PAANa, CIT, and OLNa are bound with Fe_3O_4 through the bridging bidentate, monodentate, and bridging forms, respectively (see Figure 6A−C, right). Moreover, for the Fe_3O_4@PAANa and Fe_3O_4@OLNa samples, the ISSM complex with H-bonded second carboxylate oxygen is also expected, as shown in Figure 6A,C (right).

The analysis of the Fe_3O_4@BPEI sample showed different results as BPEI was anchored to the Fe_3O_4 through amine groups. The spectrum of Fe_3O_4@BPEI is shown in Figure 6D (left). For this sample, the vibrational mode at 1106 cm^{-1} can be highlighted. This band is related to the C−N stretching[99] and is not found with the same intensity and shape in the spectrum of free BPEI (Figure 6D, left). Additionally, Bennett et al. and Sacconi et al.[100,101] reported that ammine and alkylammine complexes with iron possess a very strong vibrational mode in the region near 1150 cm^{-1}, which was also seen in the spectrum of the Fe_3O_4@BPEI sample. Thus, the increase in the C−N stretching indicates that a chemical interaction occurred between the BPEI and Fe cations present in Fe_3O_4 structure. In order to further confirm this, we measured the FTIR spectrum of a mixture of iron cations (Fe^{2+} and Fe^{3+}) and BPEI, as shown in Figure S3. The spectrum of this mixture also presented a band in the region of 1110 cm^{-1}, just as in the spectrum of the functionalized NPs. Therefore, we could affirm that the interaction between the amino groups of BPEI and Fe_3O_4 occurred through inner sphere coordination, as shown in Figure 6D (right).

Therefore, on the basis of FTIR results, we can state that the sonochemistry approach provided sufficient conditions to establish a coordination interaction between the CA and Fe_3O_4, because of the high energy induced by the implosive collapse of the cavitation bubbles.

TGA. The amount of CAs on the surface of Fe_3O_4 nanoparticles was evaluated using TGA. All of the TGA data are shown in Figure S4A−D. All of the samples had similar weight loss profiles with two events. The first was in the range of 37−190 °C and was the result of the desorption of physically adsorbed water. The second, and more significant, was observed at temperatures higher than 200 °C and was the result of the thermal decomposition of the CA molecules. The second event was used to calculate the amount of CA. The values for the Fe_3O_4@PAANa, Fe_3O_4@CIT, Fe_3O_4@OLNa, and Fe_3O_4@BPEI samples were 10.55, 15.72, 29.3, and 10.07%, respectively. These values are smaller than the theoretical amount of grafted CA molecules, which is 61%. Furthermore, the presence of a single event due to the decomposition of the organic matter suggests that the functionalized NPs possessed strongly bound CA molecules.[102] We compared our TGA results for the Fe_3O_4@PAANa and Fe_3O_4@BPEI samples with those reported in the literature for similar particles obtained by different methods.[80,81,99,103] The weight loss profile in the referenced papers presented more than one event attributed to the thermal decomposition of organic matter, which indicate the presence of weakly bound molecules on the surface of the NPs. It is worth mentioning that in these referenced publications, the TGA experiments were also performed in a N_2 atmosphere using a heating rate equal to or greater than 10 °C/min. Both FTIR and TGA results confirmed that the functionalization was successfully achieved in just 12 min through the sonochemistry approach. The high energy released in the implosive collapse of the cavitation bubbles favors the strong interaction between the iron oxide nanoparticles and the

DOI: 10.1021/acs.jpcc.7b04941
J. Phys. Chem. C 2017, 121, 24206−24222

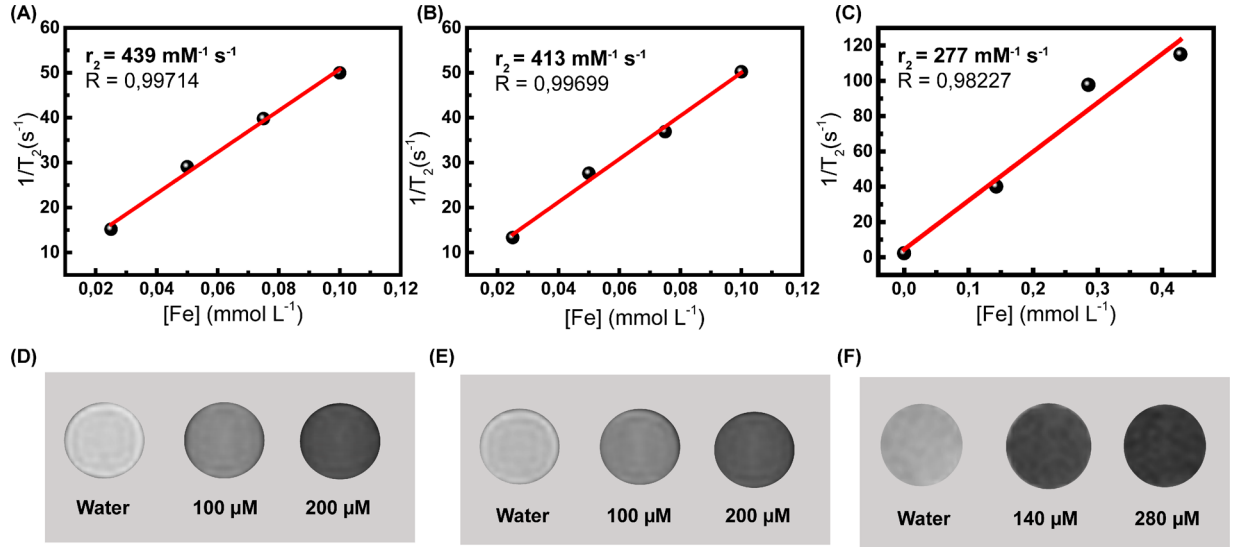

Figure 7. (Upper) Linear fittings of the inverse of the transversal relaxation time vs Fe concentration and r_2 relaxivity values for the samples (A) Fe_3O_4@PAANa, (B) Fe_3O_4@CIT, and (C) Fe_3O_4@BPEI. The fittings of the inverse of the longitudinal relaxation are shown in Figure S11. (Lower) T_2-weighted images at different concentrations of aqueous dispersions of the samples (D) Fe_3O_4@PAANa, (E) Fe_3O_4@CIT, and (F) Fe_3O_4@BPEI. Water controls were used as a reference.

CAs, resulting in a homogeneous coating on the surface of the nanoparticles. In this way, the sonochemistry synthesis represents a suitable procedure toward the improved design of tailored nanoparticles for biomedical applications, as it would reduce the toxic secondary effects derived from a weekly attached CA.[104,105]

Colloidal Properties. *DLS and Zeta Potential.* The hydrodynamic properties of aqueous dispersions of the differently coated MNPs were studied using DLS measurements. Only those MNPs stable in aqueous media were considered in the study, namely Fe_3O_4@PAANa, Fe_3O_4@CIT, and Fe_3O_4@BPEI, as listed in Table 3. All DLS size distribution curves by intensity and volume are presented in Figures S5−10. The hydrodynamic sizes of Fe_3O_4@PAANa, Fe_3O_4@BPEI, and Fe_3O_4@CIT in water are 89.4, 131.7, and 120.2 nm, respectively (Table 3). The sizes of these NPs are much greater than those obtained by XRD and TEM, as they consider the adhesion of a dipolar electric layer to the nanoparticles' surface that interact with surrounding water molecules. In addition, the organic layer allows interparticle interactions, so the formation of clusters cannot be completely excluded.[53,106] DLS measurements were also performed for aqueous solutions of the free CAs, in order to exclude the folding performed by the PAANa and BPEI (data not shown). Moreover, the polydispersity index (PDI) associated to the hydrodynamic diameters measurements were 0.079, 0.060, and 0.094 for Fe_3O_4@PAANa, Fe_3O_4@BPEI, and Fe_3O_4@CIT, respectively. These values indicate that the hydrodynamic sizes of the synthesized NPs possessed high homogeneity,[107] which is also one of the features required for biomedical applications.[108]

The zeta potential (ζ) is an important characteristic to be analyzed in relation to the colloidal stability. ζ values of Fe_3O_4@PAANa, Fe_3O_4@BPEI, and Fe_3O_4@CIT samples are listed in Table 3. The Fe_3O_4@PAANa and Fe_3O_4@CIT samples showed negative values because of the presence of carboxylate groups, which are already deprotonated at the slightly acidic pH (pH 6.0) of the water utilized. On the other hand, a positive value was observed for Fe_3O_4@BPEI (+44.5 ± 6.0 mV), which was a result of the presence of protonated amine groups at the surface of the NPs. It is worth mentioning that the borderline between stable and unstable suspensions is generally considered to be either +30 or −30 mV.[109]

However, an absolute requirement for applying these suspensions in biomedicine is stability at the high ionic strengths of physiological solutions.[104] With the exception of Fe_3O_4@PAANa, all of the samples failed to meet this requirement. In particular, in PB (pH 7.4) the particles rapidly agglomerate, reaching a *Z*-average size larger than 1000 nm (data not shown), with exception for the sample Fe_3O_4@CIT, which shows colloidal stability just in PB, but not in medium with a high salt concentration (PBS). In contrast, the Fe_3O_4@PAANa sample displayed remarkable stability in PB (pH 7.4) and even PBS. Therefore, in terms of colloidal stability, the Fe_3O_4@PAANa sample was found to be suitable for biomedical applications.

Magnetic Resonance Imaging Properties. The potential application of the synthesized NPs as an MRI contrast agent was evaluated. For these experiments, just the samples with good colloidal stability in aqueous media were selected, which were Fe_3O_4@PAANa, Fe_3O_4@BPEI, and Fe_3O_4@CIT. MNPs are traditionally considered T_2 contrast agents, as they offer a dark contrast when MR images are acquired under T_2-weighted sequences. The efficiency of an aqueous nanomaterial dispersion as a T_2-contrast agent for MRI is evaluated in terms of relaxivity, r_2. The r_2 values obtained for Fe_3O_4@PAANa, Fe_3O_4@BPEI, and Fe_3O_4@CIT aqueous dispersions after the fitting of the T_2^{-1} vs [Fe] data were 439.13, 413.13, and 277.16 $mM^{-1}\ s^{-1}$, respectively (Figure 7A−C and Table 4 entries 22−24). These values are more than 4-fold higher than those previously reported for similar functionalized magnetic nanoparticles. Table 4 (entries 1−21) lists the r_2 values found in the literature for commercial MNP-based contrast agents, as well as those prepared using the most traditional synthetic methodologies (hydrothermal, coprecipitation, thermal decomposition) and similarly functionalized with PAANa (or PAA), CIT, and BPEI (or PEI). It is also evident that the r_2 values for the samples prepared in this work are higher than those for

DOI: 10.1021/acs.jpcc.7b04941
J. Phys. Chem. C 2017, 121, 24206−24222

Table 4. Summary of Previously Reported MRI Contrast Agents Based on Fe_3O_4 NPs Prepared Using Traditional Synthetic Methodologies

entry	name	magnetic core material	core size[a] (nm)	D_{HY}[b] (nm)	shell	M_s (emu/g)	r_2[c] (mM^{-1} s^{-1})	r_2/r_1	synthetic methodology	ref
1	ferucarbotran (Resovist)	Fe_3O_4	4.2	62	carboxydextran	–	151	5.9		113
2	ferumoxides (Feridex)	Fe_3O_4, γ-Fe_2O_3	4.8–5.6	160	dextran	–	98	4.1		113
3	erumoxtran (Combidex)	Fe_3O_4	4–6	20–40	dextran	–	60	1.3		114
4	Fe_3O_4-BPEI	Fe_3O_4	11 ± 3	310	BPEI	–	137	–	hydrothermal	99
5	Fe_3O_4-BPEI 2	Fe_3O_4	12	44	BPEI	78	249	–	thermal decomposition[d]	78
6	Fe_3O_4- PEG[e]-BPEI	Fe_3O_4	10	21	PEG-BPEI	53	143	87.0	thermal decomposition[d]	115
7	Fe_3O_4–PEI[f]	Fe_3O_4	core: 9.7; clusters 200	217	PEI	70	124[g]	–	solvothermal	116
8	Fe_3O_4–Chitosan-PEI[f]	Fe_3O_4	core: 6; micelles: 50–70	65	chitosan-PEI	–	142	–	thermal decomposition[d]	117
9	Fe_3O_4–CIT	Fe_3O_4	12	30	CIT	58	102	38.0	coprecipitation	118
10	Fe_3O_4–CIT 2	Fe_3O_4	6	25	CIT	62	51.81	1.5	high-temperature salt hydrolysis followed by coprecipitation	119
11	Fe_3O_4–CIT 3	Fe_3O_4	11	35	CIT	52	73	–	hydrothermal	58
12	Fe_3O_4–CIT 4	Fe_3O_4	6	–	CIT	27	134	–	grinding the precursors in a mortar	120
13	Fe_3O_4–CIT 5	Fe_3O_4	10	150	CIT	–	156	44	coprecipitation	121
14	Fe_3O_4–CIT 5	Fe_3O_4	core: 10; clusters: 200	252	CIT	53	360[f]	–	solvothermal	116
15	MnFe-CIT	$Mn_{0.25}Fe_{0.75}Fe_2O_4$	8	–	CIT	62.4	237	–	coprecipitation	122
16	MnFe-CTAB	$MnFe_2O_4$	20	–	CTAB[h]	6	167	–	thermal decomposition[d]	123
17	Fe_3O_4-DMSA	Fe_3O_4	9	20	DMSA[i]	48	61	–	thermal decomposition[d]	124
18	Fe_3O_4-DOPA-PEG	Fe_3O_4	7	–	dopamide-PEG	46	110	–	thermal decomposition[d]	125
19	Fe_3O_4–PAA	Fe_3O_4	8–10	–	PAA	56	105	–	coprecipitation	85
20	Fe_3O_4–PAA 2	Fe_3O_4	10	172	PAA	–	232	60	coprecipitation	121
21	Fe_3O_4–PAANa	Fe_3O_4	8	90	PAANa	–	206	–	modified coprecipitation	126
22	Fe_3O_4@PAANa	Fe_3O_4	11 ± 3	89	PAANa	70.7	439	56	sonochemistry	this work
23	Fe_3O_4@BPEI	Fe_3O_4	10 ± 3	109	BPEI	70.2	277	52	sonochemistry	this work
24	Fe_3O_4@CIT	Fe_3O_4	11 ± 3	120	CIT	76.8	413	49	sonochemistry	this work

[a]Calculated by TEM or SEM. [b]Hydrodynamic diameter. [c]r_2: transverse relaxivity. [d]Thermal decomposition was used to prepare the hydrophobic NPs followed by surface ligand exchange. [e]Poly ethylene glycol. [f]Polyethylenimine. [g]0.3% of aqueous agarose gel was used as a solvent. [h]Cetyl trimethylammonium bromide. [i]DMSA: 2,3-dimercaptosuccinic acid.

Resovist, Feridex, and Combidex (Table 4, entries 1–3), which are commercial contrast agents that made it into clinics.

Furthermore, the literature reports that the core size, coating, and aggregation (hydrodynamic size) of the NPs influence the relaxivity properties of MNPs.[7,9] Thus, to perform a fair comparison between our NPs and those reported, we must consider just the NPs with similar coating agent [PAANa (or PAA), CIT, and BPEI (or PEI)] and comparable or higher core size and hydrodynamic diameter. These samples are shown in Table 4, entries 4, 7, 13, 14, 20, and 21. Therefore, it is possible to observe that the r_2 values for our NPs are greater than those of the aforementioned samples, which demonstrated the progress accomplished by the proposed method.

In order to explain the greater values observed for PAANa- and CIT- compared to the BPEI-coated NPs, it is necessary to consider the influence of the coating layer of the contrast agent. The surface of the contrast agent affects the diffusion of the water molecules around the NPs. Water molecules need to diffuse close to the magnetic core, so that they can be more efficiently influenced by the induced magnetic field of the magnetic nanoparticle. Thus, it is desirable that the coating layer interacts with water molecules in order to increase their residence time around the magnetic core.[9] According to this, the hydrophilicity of the CAs molecules attached to the nanoparticles' surface plays a key role in their relaxivity properties, in such a way that the more hydrophilic the coating is, the higher the r_2 value.[110,111] This would explain the better performance of the PAANa- and CIT-coated NPs compared to the BPEI-coated NPs (see Table 4, entries 22–24), as the carboxylate groups of PAANa and CIT provide higher hydrophilicity than the amine groups of BPEI.[112] These facts show the great potential of the proposed sonochemistry approach to prepare ferrofluids in a fast, simple, and elegant manner, while simultaneously obtaining high-quality materials.

Figure 7D–F shows the T_2-weighted MR images of a phantom containing the functionalized NPs' water dispersions

DOI: 10.1021/acs.jpcc.7b04941
J. Phys. Chem. C 2017, 121, 24206–24222

acquired at 3 T. When a T_2-weighted sequence is applied, all the samples produced a reduction of the MRI signal. As the Fe concentration increases in the solutions, the contrast gets significantly darker compared to a water control, in agreement with the high values of r_2 obtained. Similarly, the higher efficacy of the samples Fe_3O_4@PAANa and Fe_3O_4@CIT as T_2 contrast agents is evidenced, as their aqueous dispersions need lower Fe concentration to show the same contrast as in the case of Fe_3O_4@BPEI. These results highlight the suitability of the sonochemical method to achieve functionalized MNPs with excellent T_2-MRI performance in a simple and very fast way.

4. CONCLUSIONS

In summary, the sonochemistry approach proposed in this work was used to directly prepare water-dispersible functionalized Fe_3O_4 NPs with excellent magnetic, colloidal, and relaxivity properties in a simple and rapid (12 min) manner. As-synthesized coated NPs presented 8−12 nm Fe_3O_4 cores, which resulted in the transition to the superparamagnetism regime at room temperature. Moreover, the sonochemistry approach produced MNPs with high values of M_s, even after the overcoating with a nonmagnetic material. The high energy induced by ultrasound irradiation enabled covalent interaction between the CA molecules and Fe_3O_4, even though the time used in the synthesis was particularly short. Furthermore, both the carboxylate- and amine-coated NPs showed great colloidal stability in water. Emphasis must be placed on the Fe_3O_4@PAANa sample, which also exhibited colloidal stability under simulated physiological conditions. This is one of the most important requirements for in vivo applications. In addition, the MNPs obtained in this work displayed transverse relaxivity values greater than those of nanoparticulated contrast agents made of Fe oxides which were commercial or obtained using other synthetic methods. This feature clearly translated into efficient dark contrast when MR images were acquired with a T_2-weigthted sequence, confirming these MNPs as suitable T_2 contrast agents in MRI.

In particular, the methodology employed herein overcomes current synthesis-related limitations that restrain the translational research on MNPs from the bench to clinics and provides a straightforward experimental procedure that may open new avenues for the scaled up fabrication of tailored MNPs with excellent physicochemical properties suitable for biomedical applications.

■ ASSOCIATED CONTENT

Supporting Information

The Supporting Information is available free of charge on the ACS Publications website at DOI: 10.1021/acs.jpcc.7b04941.

Additional material related to FTIR, TGA, DLS size distribution curves, and linear fittings of the inverse of the longitudinal relaxation time versus Fe concentration (PDF)

■ AUTHOR INFORMATION

Corresponding Author

*E-mail: fechine@ufc.br.

ORCID

Juan Gallo: 0000-0002-2028-3234
Giuseppe Mele: 0000-0002-6684-990X
Manuel Bañobre-López: 0000-0003-4319-2631
Pierre B. A. Fechine: 0000-0002-7822-2354

Notes

The authors declare no competing financial interest.

■ ACKNOWLEDGMENTS

We gratefully acknowledge the financial support of Brazilian Agencies for Scientific and Technological Development CNPq, CAPES (Process No. 0075/14-0), and FUNCAP. We are grateful to the Microscopy and Vibrational Spectroscopy Laboratory, Advanced Functional Materials Laboratory, X-ray Laboratory of the Department of Physics − Federal University of Ceará for the FT-IR, light scattering and XRD measurements. L.C. acknowledges financial support by the Italian Ministry of Education, University and Research through the Cluster Tecnologici Regionali Project NANOAPULIA, "Nano-Photocatalysts for a Cleaner Atmosphere" (MDI6SR1 − CUP B38C14001140008). M.B.-L. is grateful to the ERDF (European Regional Development Fund) under Grant NORTE-45-2015-02. J.G. acknowledges the financial support from the Marie Curie COFUND Programme (NanoTRAINforGrowth) under Grant No. 600375. R.M.F. acknowledges financial support by Fondecyt 3170240 (Chilean agency).

■ REFERENCES

(1) Kandasamy, G.; Maity, D. Recent Advances in Superparamagnetic Iron Oxide Nanoparticles (SPIONs) for in Vitro and in Vivo Cancer Nanotheranostics. *Int. J. Pharm.* **2015**, *496*, 191−218.

(2) Ulbrich, K.; Holá, K.; Šubr, V.; Bakandritsos, A.; Tuček, J.; Zbořil, R. Targeted Drug Delivery with Polymers and Magnetic Nanoparticles: Covalent and Noncovalent Approaches, Release Control, and Clinical Studies. *Chem. Rev.* **2016**, *116*, 5338−5431.

(3) Yildiz, I. Applications of Magnetic Nanoparticles in Biomedical Separation and Purification. *Nanotechnol. Rev.* **2016**, *5*, 331−340.

(4) Beik, J.; Abed, Z.; Ghoreishi, F. S.; Hosseini-Nami, S.; Mehrzadi, S.; Shakeri-Zadeh, A.; Kamrava, S. K. Nanotechnology in Hyperthermia Cancer Therapy: From Fundamental Principles to Advanced Applications. *J. Controlled Release* **2016**, *235*, 205−221.

(5) Goodfellow, F. T.; Simchick, G. A.; Mortensen, L. J.; Stice, S. L.; Zhao, Q. Tracking and Quantification of Magnetically Labeled Stem Cells Using Magnetic Resonance Imaging. *Adv. Funct. Mater.* **2016**, *26*, 3899−3915.

(6) Gao, Z.; Ma, T.; Zhao, E.; Docter, D.; Yang, W.; Stauber, R. H.; Gao, M. Small Is Smarter: Nano MRI Contrast Agents - Advantages and Recent Achievements. *Small* **2016**, *12*, 556−576.

(7) Peng, E.; Wang, F.; Xue, J. M. Nanostructured Magnetic Nanocomposites as MRI Contrast Agents. *J. Mater. Chem. B* **2015**, *3*, 2241−2276.

(8) Lee, N.; Yoo, D.; Ling, D.; Cho, M. H.; Hyeon, T.; Cheon, J. Iron Oxide Based Nanoparticles for Multimodal Imaging and Magnetoresponsive Therapy. *Chem. Rev.* **2015**, *115*, 10637−10689.

(9) Lee, N.; Hyeon, T. Designed Synthesis of Uniformly Sized Iron Oxide Nanoparticles for Efficient Magnetic Resonance Imaging Contrast Agents. *Chem. Soc. Rev.* **2012**, *41*, 2575−2589.

(10) Frisoni, G. B.; Fox, N. C.; Jack, C. R.; Scheltens, P.; Thompson, P. M. The Clinical Use of Structural MRI in Alzheimer Disease. *Nat. Rev. Neurol.* **2010**, *6*, 67−77.

(11) Laurent, S.; Forge, D.; Port, M.; Roch, A.; Robic, C.; Vander Elst, L.; Muller, R. N. Magnetic Iron Oxide Nanoparticles: Synthesis, Stabilization, Vectorization, Physicochemical Characterizations, and Biological Applications. *Chem. Rev.* **2008**, *108*, 2064−2110.

(12) Winter, P. M.; Neubauer, A. M.; Caruthers, S. D.; Harris, T. D.; Robertson, J. D.; Williams, T. A.; Schmieder, A. H.; Hu, G.; Allen, J. S.; Lacy, E. K.; et al. Endothelial $\alpha v\beta 3$ Integrin-Targeted Fumagillin Nanoparticles Inhibit Angiogenesis in Atherosclerosis. *Arterioscler., Thromb., Vasc. Biol.* **2006**, *26*, 2103−2109.

DOI: 10.1021/acs.jpcc.7b04941
J. Phys. Chem. C 2017, 121, 24206−24222

(13) Montet, X.; Montet-Abou, K.; Reynolds, F.; Weissleder, R.; Josephson, L. Nanoparticle Imaging of Integrins on Tumor Cells. *Neoplasia* **2006**, *8*, 214−222.
(14) Nahrendorf, M.; Jaffer, F. A.; Kelly, K. A.; Sosnovik, D. E.; Aikawa, E.; Libby, P.; Weissleder, R. Noninvasive Vascular Cell Adhesion Molecule-1 Imaging Identifies Inflammatory Activation of Cells in Atherosclerosis. *Circulation* **2006**, *114*, 1504−1511.
(15) Shin, T.; Choi, Y.; Kim, S.; Cheon, J. Recent Advances in Magnetic Nanoparticle-Based Multi-Modal Imaging. *Chem. Soc. Rev.* **2015**, *44*, 4501−4516.
(16) Zhao, Z.; Zhou, Z.; Bao, J.; Wang, Z.; Hu, J.; Chi, X.; Ni, K.; Wang, R.; Chen, X.; Chen, Z.; et al. Octapod Iron Oxide Nanoparticles as High-Performance T_2 Contrast Agents for Magnetic Resonance Imaging. *Nat. Commun.* **2013**, *4*, 2266.
(17) Tong, S.; Hou, S.; Zheng, Z.; Zhou, J.; Bao, G. Coating Optimization of Superparamagnetic Iron Oxide Nanoparticles for High T_2 Relaxivity. *Nano Lett.* **2010**, *10*, 4607−4613.
(18) Brooks, R. A.; Moiny, F.; Gillis, P. On T_2-Shortening by Weakly Magnetized Particles: The Chemical Exchange Model. *Magn. Reson. Med.* **2001**, *45*, 1014−1020.
(19) Gillis, P.; Moiny, F.; Brooks, R. A. On T_2-Shortening by Strongly Magnetized Spheres: A Partial Refocusing Model. *Magn. Reson. Med.* **2002**, *47*, 257−263.
(20) Stephen, Z. R.; Dayringer, C. J.; Lim, J. J.; Revia, R. A.; Halbert, M. V.; Jeon, M.; Bakthavatsalam, A.; Ellenbogen, R. G.; Zhang, M. Approach to Rapid Synthesis and Functionalization of Iron Oxide Nanoparticles for High Gene Transfection. *ACS Appl. Mater. Interfaces* **2016**, *8*, 6320−6328.
(21) Xu, H.; Zeiger, B. W.; Suslick, K. S. Sonochemical Synthesis of Nanomaterials. *Chem. Soc. Rev.* **2013**, *42*, 2555−2567.
(22) Bang, J. H.; Suslick, K. S. Applications of Ultrasound to the Synthesis of Nanostructured Materials. *Adv. Mater.* **2010**, *22*, 1039−1059.
(23) Patil, A. B.; Bhanage, B. M. *Sonochemistry: A Greener Protocol for Nanoparticles Synthesis*; Springer International Publishing: Cham, Switzerland, 2016.
(24) Cheng, J. P.; Ma, R.; Shi, D.; Liu, F.; Zhang, X. B. Rapid Growth of Magnetite Nanoplates by Ultrasonic Irradiation at Low Temperature. *Ultrason. Sonochem.* **2011**, *18*, 1038−1042.
(25) Wu, S.; Sun, A.; Zhai, F.; Wang, J.; Xu, W.; Zhang, Q.; Volinsky, A. a Fe_3O_4 Magnetic Nanoparticles Synthesis from Tailings by Ultrasonic Chemical Co-Precipitation. *Mater. Lett.* **2011**, *65*, 1882−1884.
(26) Nazrul Islam, Md.; Van Phong, L.; Jeong, J.-R.; Kim, C. M.; Van Phong, L.; Jeong, J.-R.; Kim, C. A Facile Route to Sonochemical Synthesis of Magnetic Iron Oxide. *Thin Solid Films* **2011**, *519*, 8277−8279.
(27) Marchegiani, G.; Imperatori, P.; Mari, A.; Pilloni, L.; Chiolerio, A.; Allia, P.; Tiberto, P.; Suber, L. Sonochemical Synthesis of Versatile Hydrophilic Magnetite Nanoparticles. *Ultrason. Sonochem.* **2012**, *19*, 877−882.
(28) Zhang, S.; Zhang, Y.; Wang, Y.; Liu, S.; Deng, Y. Sonochemical Formation of Iron Oxide Nanoparticles in Ionic Liquids for Magnetic Liquid Marble. *Phys. Chem. Chem. Phys.* **2012**, *14*, 5132−5138.
(29) Abbas, M.; Takahashi, M.; Kim, C. Facile Sonochemical Synthesis of High-Moment Magnetite (Fe3O4) Nanocube. *J. Nanopart. Res.* **2013**, *15*, 1−12.
(30) Zhu, S.; Guo, J.; Dong, J.; Cui, Z.; Lu, T.; Zhu, C.; Zhang, D.; Ma, J. Sonochemical Fabrication of Fe_3O_4 Nanoparticles on Reduced Graphene Oxide for Biosensors. *Ultrason. Sonochem.* **2013**, *20*, 872−880.
(31) Martínez, H.; D'Onofrio, L.; González, G. Mössbauer Study of a Fe_3O_4/PMMA Nanocomposite Synthesized by Sonochemistry. *Hyperfine Interact.* **2014**, *224*, 99−107.
(32) Dolores, R.; Raquel, S.; Adianez, G.-L. Sonochemical Synthesis of Iron Oxide Nanoparticles Loaded with Folate and Cisplatin: Effect of Ultrasonic Frequency. *Ultrason. Sonochem.* **2015**, *23*, 391−398.
(33) Szpak, A.; Fiejdasz, S.; Prendota, W.; Strączek, T.; Kapusta, C.; Szmyd, J.; Nowakowska, M.; Zapotoczny, S. T_1-T_2 Dual-Modal MRI Contrast Agents Based on Superparamagnetic Iron Oxide Nanoparticles with Surface Attached Gadolinium Complexes. *J. Nanopart. Res.* **2014**, *16*, 2678.
(34) Freire, T. M.; Dutra, L. M. U.; Queiroz, D. C.; Ricardo, N. M. P. S.; Barreto, K.; Denardin, J. C.; Wurm, F. R.; Sousa, C. P.; Correia, A. N.; de Lima-Neto, P.; et al. Fast Ultrasound Assisted Synthesis of Chitosan-Based Magnetite Nanocomposites as a Modified Electrode Sensor. *Carbohydr. Polym.* **2016**, *151*, 760−769.
(35) Bleicher, L.; Sasaki, J. M.; Santos, C. O. P. Development of Graphical Interface for the Rietveld Refinement Program DBWS. *J. Appl. Crystallogr.* **2000**, *33*, 1189−11189.
(36) Jin, X.; Chen, X.; Cheng, Y.; Wang, L.; Hu, B.; Tan, J. Effects of Hydrothermal Temperature and Time on Hydrothermal Synthesis of Colloidal Hydroxyapatite Nanorods in the Presence of Sodium Citrate. *J. Colloid Interface Sci.* **2015**, *450*, 151−158.
(37) Tiunov, I. A.; Gorbachevskyy, M. V.; Kopitsyn, D. S.; Kotelev, M. S.; Ivanov, E. V.; Vinokurov, V. A.; Novikov, A. A. Synthesis of Large Uniform Gold and Core − Shell Gold − Silver Nanoparticles. *Effect of Temperature Control* **2016**, *90*, 152−157.
(38) Peniche, H.; Osorio, A.; Acosta, N.; de la Campa, A.; Peniche, C. Preparation and Characterization of Superparamagnetic Chitosan Microspheres: Application as a Support for the Immobilization of Tyrosinase. *J. Appl. Polym. Sci.* **2005**, *98*, 651−657.
(39) Phosphate-Buffered Saline (PBS). Cold Spring Harb. Protoc., 2006.
(40) Wu, W.; He, Q.; Jiang, C. Magnetic Iron Oxide Nanoparticles: Synthesis and Surface Functionalization Strategies. *Nanoscale Res. Lett.* **2008**, *3*, 397−415.
(41) Wu, W.; Wu, Z.; Yu, T.; Jiang, C.; Kim, W.-S. Recent Progress on Magnetic Iron Oxide Nanoparticles: Synthesis, Surface Functional Strategies and Biomedical Applications. *Sci. Technol. Adv. Mater.* **2015**, *16*, 023501.
(42) Theerdhala, S.; Bahadur, D.; Vitta, S.; Perkas, N.; Zhong, Z.; Gedanken, A. Sonochemical Stabilization of Ultrafine Colloidal Biocompatible Magnetite Nanoparticles Using Amino Acid, L-Arginine, for Possible Bio Applications. *Ultrason. Sonochem.* **2010**, *17*, 730−737.
(43) Jevtić, M.; Mitrić, M.; Škapin, S.; Jančar, B.; Ignjatović, N.; Uskoković, D. Crystal Structure of Hydroxyapatite Nanorods Synthesized by Sonochemical Homogeneous Precipitation. *Cryst. Growth Des.* **2008**, *8*, 2217−2222.
(44) Han, Y.; Wang, X.; Li, S. A Simple Route to Prepare Stable Hydroxyapatite Nanoparticles Suspension. *J. Nanopart. Res.* **2009**, *11*, 1235−1240.
(45) Sadat-Shojai, M.; Khorasani, M. T.; Dinpanah-Khoshdargi, E.; Jamshidi, A. Synthesis Methods for Nanosized Hydroxyapatite with Diverse Structures. *Acta Biomater.* **2013**, *9*, 7591−7621.
(46) Orozco-Henao, J. M.; Coral, D. F.; Muraca, D.; Moscoso-Londoño, O.; Mendoza Zélis, P.; Fernandez van Raap, M. B.; Sharma, S. K.; Pirota, K. R.; Knobel, M. Effects of Nanostructure and Dipolar Interactions on Magnetohyperthermia in Iron Oxide Nanoparticles. *J. Phys. Chem. C* **2016**, *120*, 12796−12809.
(47) Freire, R. M.; Ribeiro, T. S.; Vasconcelos, I. F.; Denardin, J. C.; Barros, E. B.; Mele, G.; Carbone, L.; Mazzetto, S. E.; Fechine, P. B. A. $MZnFe_2O_4$ (M = Ni, Mn) Cubic Superparamagnetic Nanoparticles Obtained by Hydrothermal Synthesis. *J. Nanopart. Res.* **2013**, *15*, 1616.
(48) Iyengar, S. J.; Joy, M.; Ghosh, C. K.; Dey, S.; Kotnala, R. K.; Ghosh, S. Magnetic, X-Ray and Mössbauer Studies on Magnetite/maghemite Core−shell Nanostructures Fabricated through an Aqueous Route. *RSC Adv.* **2014**, *4*, 64919−64929.
(49) Daou, T. J.; Pourroy, G.; Begin-Colin, S.; Greneche, J. M.; Ulhaq-Bouillet, C.; Legare, P.; Bernhardt, P.; Leuvrey, C.; Rogez, G. Hydrothermal Synthesis of Monodisperse Magnetite Nanoparticles. *Chem. Mater.* **2006**, *18*, 4399−4404.
(50) Baaziz, W.; Pichon, B. P.; Fleutot, S.; Liu, Y.; Lefevre, C.; Greneche, J.-M.; Toumi, M.; Mhiri, T.; Begin-Colin, S. Magnetic Iron Oxide Nanoparticles: Reproducible Tuning of the Size and Nanosized-Dependent Composition, Defects, and Spin Canting. *J. Phys. Chem. C* **2014**, *118*, 3795−3810.

DOI: 10.1021/acs.jpcc.7b04941
J. Phys. Chem. C 2017, 121, 24206−24222

(51) Santoyo Salazar, J.; Perez, L.; de Abril, O.; Truong Phuoc, L.; Ihiawakrim, D.; Vazquez, M.; Greneche, J.-M.; Begin-Colin, S.; Pourroy, G. Magnetic Iron Oxide Nanoparticles in 10−40 nm Range: Composition in Terms of Magnetite/Maghemite Ratio and Effect on the Magnetic Properties. *Chem. Mater.* **2011**, *23*, 1379−1386.
(52) Fock, J.; Bogart, L. K.; González-Alonso, D.; Espeso, J. I.; Hansen, M. F.; Varón, M.; Frandsen, C.; Pankhurst, Q. A. On the "Centre of Gravity" Method for Measuring the Composition of Magnetite/maghemite Mixtures, or the Stoichiometry of Magnetite-Maghemite Solid Solutions, via ^{57}Fe Mössbauer Spectroscopy. *J. Phys. D: Appl. Phys.* **2017**, *50*, 265005−265021.
(53) Kolen'ko, Y. V.; Bañobre-López, M.; Rodríguez-Abreu, C.; Carbó-Argibay, E.; Sailsman, A.; Piñeiro-Redondo, Y.; Cerqueira, M. F.; Petrovykh, D. Y.; Kovnir, K.; Lebedev, O. I.; et al. Large-Scale Synthesis of Colloidal Fe_3O_4 Nanoparticles Exhibiting High Heating Efficiency in Magnetic Hyperthermia. *J. Phys. Chem. C* **2014**, *118*, 8691−8701.
(54) Lu, T.; Wang, J.; Yin, J.; Wang, A.; Wang, X.; Zhang, T. Surfactant Effects on the Microstructures of Fe_3O_4 Nanoparticles Synthesized by Microemulsion Method. *Colloids Surf., A* **2013**, *436*, 675−683.
(55) Frison, R.; Cernuto, G.; Cervellino, A.; Zaharko, O.; Colonna, G. M.; Guagliardi, A.; Masciocchi, N. Magnetite−Maghemite Nanoparticles in the 5−15 nm Range: Correlating the Core−Shell Composition and the Surface Structure to the Magnetic Properties. A Total Scattering Study. *Chem. Mater.* **2013**, *25*, 4820−4827.
(56) Rodenbough, P. P.; Zheng, C.; Liu, Y.; Hui, C.; Xia, Y.; Ran, Z.; Hu, Y.; Chan, S. Lattice Expansion in Metal Oxide Nanoparticles: MgO,Co_3O_4, & Fe_3O_4. *J. Am. Ceram. Soc.* **2017**, *100*, 384−392.
(57) Salunkhe, a. B.; Khot, V. M.; Ruso, J. M.; Patil, S. I. Synthesis and Magnetostructural Studies of Amine Functionalized Superparamagnetic Iron Oxide Nanoparticles. *RSC Adv.* **2015**, *5*, 18420−18428.
(58) Wu, L.; Yang, C.; Lv, Z.; Cui, F.; Zhao, L.; Yang, P. Facile One-Pot Synthesis of Different Surfactant-Functionalized Water-Soluble Fe_3O_4 Nanoparticles as Magnetic Resonance Imaging Contrast Agents for Melanoma Tumors. *RSC Adv.* **2015**, *5*, 50557−50564.
(59) Pauly, M.; Pichon, B. P.; Panissod, P.; Fleutot, S.; Rodriguez, P.; Drillon, M.; Begin-Colin, S. Size Dependent Dipolar Interactions in Iron Oxide Nanoparticle Monolayer and Multilayer Langmuir-Blodgett Films. *J. Mater. Chem.* **2012**, *22*, 6343−6350.
(60) Witte, K.; Bodnar, W.; Mix, T.; Schell, N.; Fulda, G.; Woodcock, T. G.; Burkel, E. A Detailed Study on the Transition from the Blocked to the Superparamagnetic State of Reduction-Precipitated Iron Oxide Nanoparticles. *J. Magn. Magn. Mater.* **2016**, *403*, 103−113.
(61) Daou, T. J.; Pourroy, G.; Greneche, J. M.; Bertin, A.; Felder-Flesch, D.; Begin-Colin, S. Water Soluble Dendronized Iron Oxide Nanoparticles. *Dalton Trans.* **2009**, *23*, 4442−4449.
(62) Zélis, P. M.; Pasquevich, G. a.; Stewart, S. J.; Raap, M. B. F. v.; Aphesteguy, J.; Bruvera, I. J.; Laborde, C.; Pianciola, B.; Jacobo, S.; Sánchez, F. H. Structural and Magnetic Study of Zinc-Doped Magnetite Nanoparticles and Ferrofluids for Hyperthermia Applications. *J. Phys. D: Appl. Phys.* **2013**, *46*, 125006−125018.
(63) León-Félix, L.; Chaker, J.; Parise, M.; Coaquira, J. A. H.; De Los Santos Valladares, L.; Bustamante, A.; Garg, V. K.; Oliveira, A. C.; Morais, P. C. Synthesis and Characterization of Uncoated and Gold-Coated Magnetite Nanoparticles. *Hyperfine Interact.* **2014**, *224*, 179−188.
(64) Gerber, O.; Pichon, B. P.; Ulhaq, C.; Grenèche, J.-M.; Lefevre, C.; Florea, I.; Ersen, O.; Begin, D.; Lemonnier, S.; Barraud, E.; et al. Low Oxidation State and Enhanced Magnetic Properties Induced by Raspberry Shaped Nanostructures of Iron Oxide. *J. Phys. Chem. C* **2015**, *119*, 24665−24673.
(65) Bhattacharya, S.; Roychowdhury, A.; Tiwari, V.; Prasad, A.; Ningthoujam, R. S.; Patel, A. B.; Das, D.; Nayar, S. Effect of Biomimetic Templates on the Magneto-Structural Properties of Fe_3O_4 Nanoparticles. *RSC Adv.* **2015**, *5*, 13777−13786.
(66) Fleutot, S.; Nealon, G. L.; Pauly, M.; Pichon, B. P.; Leuvrey, C.; Drillon, M.; Gallani, J.-L.; Guillon, D.; Donnio, B.; Begin-Colin, S. Spacing-Dependent Dipolar Interactions in Dendronized Magnetic Iron Oxide Nanoparticle 2D Arrays and Powders. *Nanoscale* **2013**, *5*, 1507−1516.
(67) Mikhaylova, M.; Kim, D. K.; Bobrysheva, N.; Osmolowsky, M.; Semenov, V.; Tsakalakos, T.; Muhammed, M. Superparamagnetism of Magnetite Nanoparticles: Dependence on Surface Modification. *Langmuir* **2004**, *20*, 2472−2477.
(68) Chen, Y.-L.; Yang, D.-P. *Mössbauer Effect in Lattice Dynamics: Experimental Techniques and Applications*; WILEY-VCH Verlag GmbH & Co. KGaA: Weinheim, Germany, 2007.
(69) Shipilin, M. A.; Zakharova, I. N.; Shipilin, A. M.; Bachurin, V. I. Mössbauer Studies of Magnetite Nanoparticles. *J. Surf. Invest.: X-Ray, Synchrotron Neutron Tech.* **2014**, *8*, 557−561.
(70) Roca, A. G.; Marco, J. F.; Morales, M. d. P.; Serna, C. J. Effect of Nature and Particle Size on Properties of Uniform Magnetite and Maghemite Nanoparticles. *J. Phys. Chem. C* **2007**, *111*, 18577−18584.
(71) Ushakov, M. V.; Oshtrakh, M. I.; Felner, I.; Semenova, A. S.; Kellerman, D. G.; Šepelák, V.; Semionkin, V. A.; Morais, P. C. Magnetic Properties of Iron Oxide-Based Nanoparticles: Study Using Mössbauer Spectroscopy with a High Velocity Resolution and Magnetization Measurements. *J. Magn. Magn. Mater.* **2017**, *431*, 46−48.
(72) Mørup, S.; Topsøe, H.; Lipka, J. Modified Theory for Mössbauer Spectra of Superparamagnetic Particles : Application to Fe_3O_4. *J. Phys. Colloq.* **1976**, *37*, 287−290.
(73) Arévalo, P.; Isasi, J.; Caballero, A. C.; Marco, J. F.; Martín-Hernández, F. Magnetic and Structural Studies of Fe_3O_4 Nanoparticles Synthesized via Coprecipitation and Dispersed in Different Surfactants. *Ceram. Int.* **2017**, *43*, 10333−10340.
(74) da Silva, S. W.; Guilherme, L. R.; de Oliveira, A. C.; Garg, V. K.; Rodrigues, P. A. M.; Coaquira, J. A. H.; da Silva Ferreira, Q.; de Melo, G. H. F.; Lengyel, A.; Szalay, R.; et al. Mössbauer and Raman Spectroscopic Study of Oxidation and Reduction of Iron Oxide Nanoparticles Promoted by Various Carboxylic Acid Layers. *J. Radioanal. Nucl. Chem.* **2017**, *312*, 111−119.
(75) da Costa, G. M.; Blanco-Andujar, C.; De Grave, E.; Pankhurst, Q. A. Magnetic Nanoparticles for in Vivo Use: A Critical Assessment of Their Composition. *J. Phys. Chem. B* **2014**, *118*, 11738−11746.
(76) Kolen'ko, Y. V.; Bañobre-López, M.; Rodríguez-Abreu, C.; Carbó-Argibay, E.; Deepak, F. L.; Petrovykh, D. Y.; Cerqueira, M. F.; Kamali, S.; Kovnir, K.; Shtansky, D. V.; et al. High-Temperature Magnetism as a Probe for Structural and Compositional Uniformity in Ligand-Capped Magnetite Nanoparticles. *J. Phys. Chem. C* **2014**, *118*, 28322−28329.
(77) Gerber, O.; Pichon, B. P.; Ulhaq, C.; Grenèche, J.-M.; Lefevre, C.; Florea, I.; Ersen, O.; Begin, D.; Lemonnier, S.; Barraud, E.; Begin-colin, S. Low Oxidation State and Enhanced Magnetic Properties Induced by Raspberry Shaped Nanostructures of Iron Oxide. *J. Phys. Chem. C* **2015**, *119*, 24665−24673.
(78) Mohapatra, J.; Mitra, A.; Tyagi, H.; Bahadur, D.; Aslam, M. Iron Oxide Nanorods as High-Performance Magnetic Resonance Imaging Contrast Agents. *Nanoscale* **2015**, *7*, 9174−9184.
(79) Li, Z.; Sun, Q.; Gao, M. Preparation of Water-Soluble Magnetite Nanocrystals from Hydrated Ferric Salts in 2-Pyrrolidone: Mechanism Leading to Fe3O4. *Angew. Chem., Int. Ed.* **2005**, *44*, 123−126.
(80) Calatayud, M. P.; Sanz, B.; Raffa, V.; Riggio, C.; Ibarra, M. R.; Goya, G. F. The Effect of Surface Charge of Functionalized Fe_3O_4 Nanoparticles on Protein Adsorption and Cell Uptake. *Biomaterials* **2014**, *35*, 6389−6399.
(81) Li, J.; Hu, Y.; Yang, J.; Sun, W.; Cai, H.; Wei, P.; Sun, Y.; Zhang, G.; Shi, X.; Shen, M. Facile Synthesis of Folic Acid-Functionalized Iron Oxide Nanoparticles with Ultrahigh Relaxivity for Targeted Tumor MR Imaging. *J. Mater. Chem. B* **2015**, *3*, 5720−5730.
(82) Wang, Y.; Xu, F.; Zhang, L.; Wei, X. One-Pot Solvothermal Synthesis of Fe_3O_4−PEI Composite and its Further Modification with Au Nanoparticles. *J. Nanopart. Res.* **2013**, *15*, 1338.
(83) Petcharoen, K.; Sirivat, A. Synthesis and Characterization of Magnetite Nanoparticles via the Chemical Co-Precipitation Method. *Mater. Sci. Eng., B* **2012**, *177*, 421−427.

DOI: 10.1021/acs.jpcc.7b04941
J. Phys. Chem. C 2017, 121, 24206−24222

(84) Schladt, T. D.; Schneider, K.; Schild, H.; Tremel, W. Synthesis and Bio-Functionalization of Magnetic Nanoparticles for Medical Diagnosis and Treatment. *Dalton Trans.* **2011**, *40*, 6315−6343.
(85) Gupta, J.; Mohapatra, J.; Bhargava, P.; Bahadur, D. A pH-Responsive Folate Conjugated Magnetic Nanoparticle for Targeted Chemo-Thermal Therapy and MRI Diagnosis. *Dalt. Trans.* **2016**, *45*, 2454−2461.
(86) Shen, W.; Shi, M.; Wang, M.; Chen, H. A Simple Synthesis of Fe_3O_4 Nanoclusters and Their Electromagnetic Nanocomposites with Polyaniline. *Mater. Chem. Phys.* **2010**, *122*, 588−594.
(87) Nigam, S.; Barick, K. C.; Bahadur, D. Development of Citrate-Stabilized Fe_3O_4 Nanoparticles: Conjugation and Release of Doxorubicin for Therapeutic Applications. *J. Magn. Magn. Mater.* **2011**, *323*, 237−243.
(88) Lu, W.; Ling, M.; Jia, M.; Huang, P.; Li, C.; Yan, B. Facile Synthesis and Characterization of Polyethylenimine-Coated Fe_3O_4 Superparamagnetic Nanoparticles for Cancer Cell Separation. *Mol. Med. Rep.* **2014**, *9*, 1080−1084.
(89) Ang, D.; Tay, C. Y.; Tan, L. P.; Preiser, P. R.; Ramanujan, R. V. Vitro Studies of Magnetically Enhanced Transfection in COS-7 Cells. *Mater. Sci. Eng., C* **2011**, *31*, 1445−1457.
(90) Guardia, P.; Labarta, A.; Batlle, X. Tuning the Size, the Shape, and the Magnetic Properties of Iron Oxide Nanoparticles. *J. Phys. Chem. C* **2011**, *115*, 390−396.
(91) Daou, T. J.; Begin-Colin, S.; Grenèche, J. M.; Thomas, F.; Derory, A.; Bernhardt, P.; Legaré, P.; Pourroy, G. Phosphate Adsorption Properties of Magnetite-Based Nanoparticles. *Chem. Mater.* **2007**, *19*, 4494−4505.
(92) Schwaminger, S. P.; García, P. F.; Merck, G. K.; Bodensteiner, F. A.; Heissler, S.; Günther, S.; Berensmeier, S. Nature of Interactions of Amino Acids with Bare Magnetite Nanoparticles. *J. Phys. Chem. C* **2015**, *119*, 23032−23041.
(93) Pujari, S. P.; Scheres, L.; Marcelis, A. T. M.; Zuilhof, H. Covalent Surface Modification of Oxide Surfaces. *Angew. Chem., Int. Ed.* **2014**, *53*, 6322−6356.
(94) Jovanović, S.; Spreitzer, M.; Tramšek, M.; Trontelj, Z.; Suvorov, D. Effect of Oleic Acid Concentration on the Physicochemical Properties of Cobalt Ferrite Nanoparticles. *J. Phys. Chem. C* **2014**, *118*, 13844−13856.
(95) Baccile, N.; Noiville, R.; Stievano, L.; Van Bogaert, I. Sophorolipids-Functionalized Iron Oxide Nanoparticles. *Phys. Chem. Chem. Phys.* **2013**, *15*, 1606−1620.
(96) Nakamoto, K. *Infrared and Raman Spectra of Inorganic and Coordination Compounds: Part B: Applications in Coordination, Organometallic, and Bioinorganic Chemistry*; John Wiley & Sons, Inc.: Hoboken, NJ, 2008.
(97) Lenz, A.; Selegård, L.; Söderlind, F.; Larsson, A.; Holtz, P. O.; Uvdal, K.; Ojamäe, L.; Käll, P. O. ZnO Nanoparticles Functionalized with Organic Acids: An Experimental and Quantum-Chemical Study. *J. Phys. Chem. C* **2009**, *113*, 17332−17341.
(98) Chernyshova, I. V.; Ponnurangam, S.; Somasundaran, P. Adsorption of Fatty Acids on Iron (Hydr)oxides from Aqueous Solutions. *Langmuir* **2011**, *27*, 10007−10018.
(99) Cai, H.; An, X.; Cui, J.; Li, J.; Wen, S.; Li, K.; Shen, M.; Zheng, L.; Zhang, G.; Shi, X. Facile Hydrothermal Synthesis and Surface Functionalization of Polyethyleneimine-Coated Iron Oxide Nanoparticles for Biomedical Applications. *ACS Appl. Mater. Interfaces* **2013**, *5*, 1722−1731.
(100) Sacconi, L.; Sabatini, A.; Gans, P. Infrared Spectra from 80 to 2000 cm^{-1} of Some Metal-Ammine Complexes. *Inorg. Chem.* **1964**, *3*, 1772−1774.
(101) Bennett, A. M. A.; Foulds, G. A.; Thornton, D. A.; Watkins, G. M. The Infrared Spectra of Ethylenediamine complexes—II. Tris-, Bis- and Mono(ethylenediamine) Complexes of metal(II) Halides. *Spectrochim. Acta Part A Mol. Spectrosc.* **1990**, *46*, 13−22.
(102) Shen, L.; Laibinis, P. E.; Hatton, T. A. Bilayer Surfactant Stabilized Magnetic Fluids: Synthesis and Interactions at Interfaces. *Langmuir* **1999**, *15*, 447−453.
(103) Liu, S.; Lu, F.; Jia, X.; Cheng, F.; Jiang, L.-P.; Zhu, J.-J. Microwave-Assisted Synthesis of a Biocompatible Polyacid-Conjugated Fe_3O_4 Superparamagnetic Hybrid. *CrystEngComm* **2011**, *13*, 2425−2429.
(104) Amstad, E.; Textor, M.; Reimhult, E. Stabilization and Functionalization of Iron Oxide Nanoparticles for Biomedical Applications. *Nanoscale* **2011**, *3*, 2819.
(105) Rahimi, M.; Yousef, M.; Cheng, Y.; Meletis, E. I.; Eberhart, R. C.; Nguyen, K. Formulation and Characterization of a Covalently Coated Magnetic Nanogel. *J. Nanosci. Nanotechnol.* **2009**, *9*, 4128−4134.
(106) Ditsch, A.; Laibinis, P. E.; Wang, D. I. C.; Hatton, T. A. Controlled Clustering and Enhanced Stability of Polymer-Coated Magnetic Nanoparticles. *Langmuir* **2005**, *21*, 6006−6018.
(107) Lan, F.; Liu, K.-X.; Jiang, W.; Zeng, X.-B.; Wu, Y.; Gu, Z.-W. Facile Synthesis of Monodisperse Superparamagnetic Fe_3O_4/PMMA Composite Nanospheres with High Magnetization. *Nanotechnology* **2011**, *22*, 225604−225611.
(108) Gao, J.; Gu, H.; Xu, B. Multifunctional Magnetic Nanoparticles: Design, Synthesis, and Biomedical Applications. *Acc. Chem. Res.* **2009**, *42*, 1097−1107.
(109) Hunter, R. J. *Zeta Potential in Colloid Science: Principles and Applications*; Academic Press Inc.: San Diego, CA, 2013.
(110) Huang, C.-C.; Chuang, K.-Y.; Chou, C.-P.; Wu, M.-T.; Sheu, H.-S.; Shieh, D.-B.; Tsai, C.-Y.; Su, C.-H.; Lei, H.-Y.; Yeh, C.-S. Size-Control Synthesis of Structure Deficient Truncated Octahedral $Fe_{3-\delta}O_4$ Nanoparticles: High Magnetization Magnetites as Effective Hepatic Contrast Agents. *J. Mater. Chem.* **2011**, *21*, 7472−7479.
(111) Duan, H.; Kuang, M.; Wang, X.; Wang, Y. A.; Mao, H.; Nie, S. Reexamining the Effects of Particle Size and Surface Chemistry on the Magnetic Properties of Iron Oxide Nanocrystals: New Insights into Spin Disorder and Proton Relaxivity. *J. Phys. Chem. C* **2008**, *112*, 8127−8131.
(112) Zheng, X.-Y.; Zhao, K.; Tang, J.; Wang, X.-Y.; Li, L.-D.; Chen, N.-X.; Wang, Y.-J.; Shi, S.; Zhang, X.; Malaisamy, S.; et al. Gd-Dots with Strong Ligand−Water Interaction for Ultrasensitive Magnetic Resonance Renography. *ACS Nano* **2017**, *11*, 3642−3650.
(113) Wang, Y.-X. J.; Hussain, S. M.; Krestin, G. P. Superparamagnetic Iron Oxide Contrast Agents: Physicochemical Characteristics and Applications in MR Imaging. *Eur. Radiol.* **2001**, *11*, 2319−2331.
(114) Wang, Y.-X. J. Superparamagnetic Iron Oxide Based MRI Contrast Agents: Current Status of Clinical Application. *Quant. Imaging Med. Surg.* **2011**, *1*, 35−40.
(115) Wang, J.; Zhang, B.; Wang, L.; Wang, M.; Gao, F. One-Pot Synthesis of Water-Soluble Superparamagnetic Iron Oxide Nanoparticles and Their MRI Contrast Effects in the Mouse Brains. *Mater. Sci. Eng., C* **2015**, *48*, 416−423.
(116) Xu, F.; Cheng, C.; Xu, F.; Zhang, C.; Xu, H.; Xie, X.; Yin, D.; Gu, H. Superparamagnetic Magnetite Nanocrystal Clusters: A Sensitive Tool for MR Cellular Imaging. *Nanotechnology* **2009**, *20*, 405102−405112.
(117) Wang, C.; Ravi, S.; Martinez, G. V.; Chinnasamy, V.; Raulji, P.; Howell, M.; Davis, Y.; Mallela, J.; Seehra, M. S.; Mohapatra, S. Dual-Purpose Magnetic Micelles for MRI and Gene Delivery. *J. Controlled Release* **2012**, *163*, 82−92.
(118) Saraswathy, A.; Nazeer, S. S.; Jeevan, M.; Nimi, N.; Arumugam, S.; Harikrishnan, V. S.; Varma, P. R.; Jayasree, R. S. Citrate Coated Iron Oxide Nanoparticles with Enhanced Relaxivity for in Vivo Magnetic Resonance Imaging of Liver Fibrosis. *Colloids Surf., B* **2014**, *117*, 216−224.
(119) Srivastava, S.; Awasthi, R.; Gajbhiye, N. S.; Agarwal, V.; Singh, A.; Yadav, A.; Gupta, R. K. Innovative Synthesis of Citrate-Coated Superparamagnetic Fe_3O_4 Nanoparticles and Its Preliminary Applications. *J. Colloid Interface Sci.* **2011**, *359*, 104−111.
(120) Wang, Z.; Zhao, L.; Yang, P.; Lv, Z.; Sun, H.; Jiang, Q. Water-Soluble Amorphous Iron Oxide Nanoparticles Synthesized by a Quickly Pestling and Nontoxic Method at Room Temperature as MRI Contrast Agents. *Chem. Eng. J.* **2014**, *235*, 231−235.

DOI: 10.1021/acs.jpcc.7b04941
J. Phys. Chem. C 2017, 121, 24206−24222

(121) Jedlovszky-Hajdú, A.; Tombácz, E.; Bányai, I.; Babos, M.; Palkó, A. Carboxylated Magnetic Nanoparticles as MRI Contrast Agents: Relaxation Measurements at Different Field Strengths. *J. Magn. Magn. Mater.* **2012**, *324*, 3173−3180.
(122) Ereath Beeran, A.; Nazeer, S. S.; Fernandez, F. B.; Muvvala, K. S.; Wunderlich, W.; Anil, S.; Vellappally, S.; Ramachandra Rao, M. S.; John, A.; Jayasree, R. S.; et al. An Aqueous Method for the Controlled Manganese (Mn^{2+}) Substitution in Superparamagnetic Iron Oxide Nanoparticles for Contrast Enhancement in MRI. *Phys. Chem. Chem. Phys.* **2015**, *17*, 4609−4619.
(123) Yang, G.; He, F.; Lv, R.; Gai, S.; Cheng, Z.; Dai, Y.; Yang, P. A Cheap and Facile Route to Synthesize Monodisperse Magnetic Nanocrystals and Their Application as MRI Agents. Dalt. *Trans* **2015**, *44*, 247−253.
(124) Song, M.; Zhang, Y.; Hu, S.; Song, L.; Dong, J.; Chen, Z.; Gu, N. Influence of Morphology and Surface Exchange Reaction on Magnetic Properties of Monodisperse Magnetite Nanoparticles. *Colloids Surf., A* **2012**, *408*, 114−121.
(125) Smolensky, E. D.; Park, H.-Y. E.; Berquó, T. S.; Pierre, V. C. Surface Functionalization of Magnetic Iron Oxide Nanoparticles for MRI Applications - Effect of Anchoring Group and Ligand Exchange Protocol. *Contrast Media Mol. Imaging* **2011**, *6*, 189−199.
(126) Santra, S.; Kaittanis, C.; Grimm, J.; Perez, J. M. Drug/dye-Loaded, Multifunctional Iron Oxide Nanoparticles for Combined Targeted Cancer Therapy and Dual Optical/magnetic Resonance Imaging. *Small* **2009**, *5*, 1862−1868.

DOI: 10.1021/acs.jpcc.7b04941
J. Phys. Chem. C 2017, 121, 24206−24222